Journal of Inorganic Biochemistry 279 (2026) 113259

Contents lists available at ScienceDirect

Journal of Inorganic Biochemistry

journal homepage: www.elsevier.com/locate/jinorgbio

Formation and spontaneous oxidation of neutral [4Fe–4S] clusters in prebiotic oceans☆

Theodore M. Present [a,*], Joan Selverstone Valentine [b], Jena E. Johnson [c], Robert K. Szilagyi [d]

[a] Division of Geological and Planetary Science, California Institute of Technology, Pasadena, CA 91125, USA
[b] Department of Chemistry and Biochemistry, UCLA, Los Angeles, CA 90095, USA
[c] Department of Earth and Environmental Sciences, University of Michigan, Ann Arbor, MI 48109, USA
[d] Department of Chemistry, The University of British Columbia - Okanagan, Kelowna, BC V1V 1V7, Canada

ARTICLE INFO

Keywords:
Archean ferruginous oceans
iron-sulfur proteins
[4Fe–4S] cubane clusters
mackinawite nanoparticle sheets
density functional theory
PHREEQC reaction network modeling

ABSTRACT

Iron-sulfur clusters are enzyme cofactors essential to life and are proposed to form the basis of earliest metabolisms. Fe–S rhomb and cubane clusters require both Fe(II) and Fe(III) for stability, but the Archean ocean was dominated by reduced Fe(II). We hypothesize that protons could have served as an oxidant of Fe(II) to Fe(III) during cluster assembly. Concomitantly, coordinating ligands that complete the tetrahedral geometry of the iron sites in the molecular cubane clusters may have assured cluster stability and facilitated proton reduction. Density functional theory calculations suggest that protons delivered by H_3O^+, $Fe(SH)^+$, or H_2S can oxidize [2Fe–2S] clusters and promote the formation of cationic [4Fe–4S] clusters. The relative energetics of mackinawite-like $(FeS)_n$(aq) neutral nanoparticle sheets and ligated cationic [4Fe–4S] cubanes further indicate that ligands, such as water, bisulfide, and bioligands (such as short peptides) indeed play a key role in trapping cubane cluster states along the process of mackinawite-like nanoparticle sheet formation. Together, the redox reaction by protons and ligand coordination could have enabled molecular Fe–S cluster cofactor assembly directly from the Fe(II)-rich, sulfide-bearing waters of early Earth.

1. Introduction

Early life evolved in anoxic, ferrous iron-rich oceans, whose chemical composition was the primary environmental factor that shaped life's abilities [1–7]. Metal cofactors, ultimately derived from the environment, are essential components in enzymes and other biomolecules and enable a rich suite of biological functions. Today, magnesium, zinc, and iron are the dominant metallic cofactors in all enzyme classes [8]. It has been hypothesized that, in the absence of highly-evolved metal acquisition, homeostasis, and tetrapyrrole synthesis pathways, early life could have fulfilled all of its necessary functions solely with Fe(II) [1,9]. In addition to sophisticated heme cofactors, entirely inorganic iron cofactors serve as the active sites in rubredoxins (a single Fe) and polynuclear ferredoxins, which include [2Fe–2S] rhombs and [4Fe–4S] cubane molecular clusters. Modern organisms widely use rubredoxins, ferredoxins, and high-potential iron-sulfur proteins for electron transport. Ferredoxins enable redox catalysis, radical chemistry, small molecule activation, molecular sensing, and cell signaling, in addition to Fe–S clusters even serving structural functions in some proteins [10–13]. Given this functional diversity in extant biology, a broad primordial array of capabilities was possible if earliest life used Fe–S clusters as proto-ferredoxin cofactors [1,14–18].

The similarities between Fe–S clusters and minerals like greigite, mackinawite, or pyrite initially motivated the hypothesis that proto-ferredoxins derived from these minerals [14–16], although subsequent work has emphasized the diversity of biological cofactors and important differences between them and minerals [11,19]. Furthermore, the chemical reactivity and catalytic capabilities of molecular clusters form the basis for the 'iron-sulfur world' hypothesis for the origin of life [14,15,18,20]. Fe–S clusters form two distinct geometric structures from iron- and sulfur-rich fluids: three-dimensional [4Fe–4S] molecular cubanes and two-dimensional mackinawite-like sheets comprised of $(FeS)_2$ rhombs and their polymers (Fig. 1). This structural distinction has fundamental implications for biological accessibility. The nanosheets of $(FeS)_n$(aq), $n < 150$, are precursors to the formation of the mineral phases [21–25], which precipitate from solution and become less

☆ This article is part of a Special issue entitled: 'Harry Gray Special Issue' published in Journal of Inorganic Biochemistry.

* Corresponding author.
E-mail address: tpresent@caltech.edu (T.M. Present).

https://doi.org/10.1016/j.jinorgbio.2026.113259
Received 30 October 2025; Received in revised form 17 December 2025; Accepted 4 February 2026
Available online 5 February 2026

available to primitive organisms. In contrast, discrete molecular cubanes are dissolved clusters that can bind organic ligands such as short peptides and form proto-ferredoxins.

Central to their electron transport and chemical reactivity, the clusters can adopt an oxidation state continuum from 'super-reduced' to fully oxidized forms, e.g., $[2Fe–2S]^{0}$ to $[2Fe–2S]^{2+}$ and $[4Fe–4S]^{0}$ to $[4Fe–4S]^{4+}$ [26]. Their reduction potentials are poised by their inner and outer-sphere coordination environment in a range from −500 mV to +700 mV in plant ferredoxins (rhombs) and high potential iron-proteins (cubanes) [25–31]. Recently, it has been proposed that the various redox states differ predominantly by the oxidation state of the sulfur centers [32]. However, the 'super-reduced' cubanes are unstable, transient species in aqueous solutions, and they decay to mackinawite-like nanosheets or precipitates unless they are stabilized by coordinating ligands like thiolates [26,29,33]. The assembly of the [4Fe–4S] cubanes like those in bacterial ferredoxins requires the availability of ferric iron or elemental sulfur [25,34–39], and the formation of specific cluster geometries and stoichiometries depend on the availability of Fe and S ions in solution [40]. Cubanes are commonly synthesized in the lab, often in non-aqueous solvents [27,38], from Fe(III) and excess reductants such as β-mercaptoethanol, cysteine, or glutathione; these also serve as cluster stabilizing ligands involving a series of intermediates that include mononuclear iron thiolates and binuclear rhombs [25,27,29,38,40].

Our central question is how emerging life accessed and harvested clusters from the aqueous environment. Before evolution could explore and exploit the chemical capabilities of Fe–S clusters, early organisms would have needed sufficiently frequent encounters with environmental clusters in sufficiently high concentrations to experience their reactivity. Only then could evolutionary pressures select for mechanisms to control, regulate, and acquire these cofactors with primitive bioligands [1]. While local environments may have contained enough Fe(III) to support cluster assembly [34], the instability of clusters in the reducing, ferrous iron-rich earliest oceans posed a significant challenge for earliest life to evolve and spread. As Earth's oceans oxygenated, beginning approximately 2.5 Ga, iron-sulfur cluster biosynthesis pathways would have become more sophisticated, permitting selective uptake, incorporation, chaperoning, and regulation of Fe(II) and Fe(III) [11,41,42].

An alternative mechanism to assemble Fe–S clusters derives from their functional diversity. Specific Fe–S cluster containing metalloenzymes are capable of reducing protons, dinitrogen, or oxidizing dihydrogen (hydrogenases and nitrogenases) [17,43,44], as well as

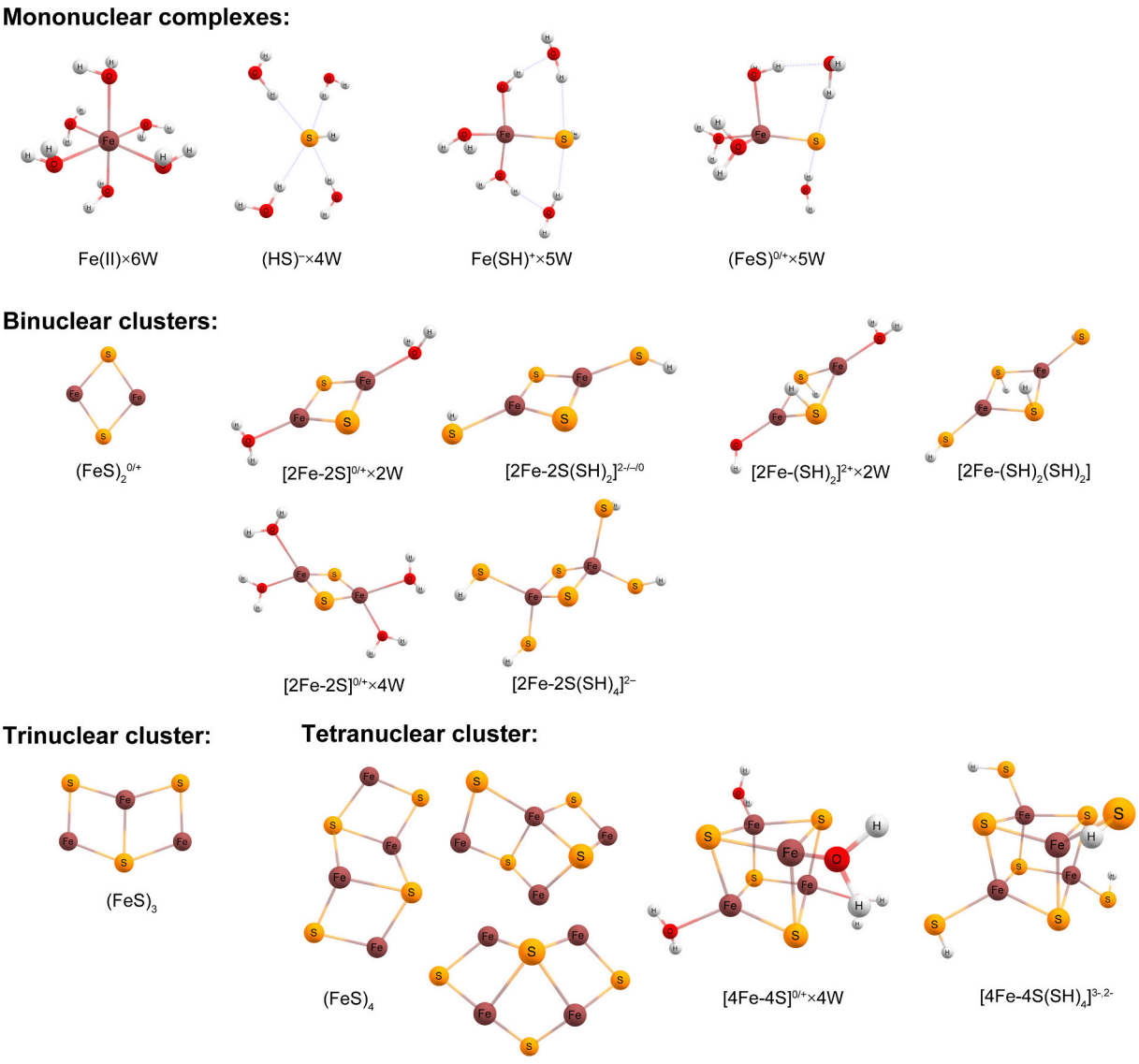

Fig. 1. Structural representations of the important species considered in this study of the competitive formation of mackinawite-like 2D nanosheets, molecular rhombs, and 3D cubanes.

reversibly interconverting carbon monoxide to carbon dioxide in the presence of Ni as heterometal [45]. The role of these 'great metalloclusters of biology' [19] in dihydrogen evolution and uptake reactions suggests that a proton can be an oxidizing agent for interconversion between the super-reduced cluster and oxidized, cationic cluster states [15,16]. Oxidation of ferrous clusters by hydrogen sulfide is a S-based redox pathway towards the formation of pyrite with persulfide (S_2^{2-}) [46,47], and is analogous to the oxidation of Fe(II) by water in serpentinization reactions [48–50]. In these pathways, hydrogen sulfide is the species that delivers the oxidizing power of a proton to the cluster, while the bisulfide ion formed upon ionization can provide an in-situ ligand for stabilizing the Fe(III) containing cluster.

In early ferrous iron-rich oceans, we hypothesize that protons were an adequately strong and environmentally abundant oxidant to help form cationic clusters directly from Fe(II) and HS^- without the need for the presence of abundant Fe(III). We propose that the accumulation of these clusters may have been facilitated by the stabilizing effect of coordinating ligands, such as bisulfide and similar environmental molecular ions. Once formed and stable with sufficient lifetimes, the strong affinities of Fe–S clusters to chelating thiolate/cysteine-rich ligands could have promoted the emergence of proto-ferredoxins [14,15,17,51–54].

To begin to test this hypothesis and map out the availability of Fe–S cluster species, we investigated the thermodynamics of Fe–S cluster assembly and small molecule/ion ligation with density functional theory (DFT) calculations and equilibrium reaction network modeling. While both computational approaches have their limitations in complex aqueous solutions like earliest seawater, their combined approach provides a framework for experimentally testable constraints for future laboratory experiments. Furthermore, a unique approach to our modeling strategy is that we did not assume the presence of any oxidized species often considered as starting points (e.g., [55]), and rather we explored reaction networks that lead to the formation of ferric iron along spontaneous or close to spontaneous processes.

2. Methods

2.1. DFT calculations

Quantum chemical calculations of speciation for Fe and S ions, $(FeS)_n$ oligomers, and various molecular Fe–S clusters were carried out using a thermodynamically validated level of theory that describes the electron/electron and electron/nuclear interactions based on electron density (density functional). Once the potential energy of each molecule or ion is determined, we utilized statistical thermodynamic relationships to connect the 0 K, 0 atm simulation results with thermodynamic observables, such as free energy and enthalpy, at 298 K, 1 atm, and pH = 0 standard state. For consistency in differentiating various species, we use square brackets to designate molecular rhomb and cubane structures of [2Fe–2S] and [4Fe–4S] clusters. The $(FeS)_n$ notation corresponds to mackinawite-like electroactive nanoparticle sheets (nanosheets). The main difference between the molecular clusters and nanosheets is the number of neighbors for the sulfide ligands. In the [2Fe–2S] and [4Fe–4S] molecular clusters, the bridging sulfur connects two-(μ^2) or three-(μ^3) iron centers, while in the two-dimensional nanosheets, the tetrahedral irons are surrounded by four-coordinate (μ^4) sulfide ions. The $n = 2$ member of both series serves as a branching point (Fig. 1), since the non-ligated [2Fe–2S] cluster is structurally and stoichiometrically identical to $(FeS)_2$.

A spectroscopically calibrated functional using Fe–S bonding information from X-ray absorption spectroscopic measurements has been defined for [4Fe–4S] clusters (BP86 functional with 5% HF exchange) [56,57]. However, we needed a unified theory that can describe accurately the solvated proton, proton reduction, hydrogen sulfide deprotonation, and pK_a changes of coordinated water to ferrous and ferric ions. Therefore, we assessed the performance of 97 functionals that included pure GGA functionals, hybrids and double-hybrids, range-separated and dispersion corrected functionals. By using the entire repertoire of functionals, we were able to gauge the chemical accuracy of the calculated equilibrium reactions to simultaneously describe all the above processes, and to critique the chemical reactions that have been proposed for the experimental equilibrium constants. We considered anionic species, H-bonding, coordinative bonding, and radicals. Therefore, we selected the def2TZVPPD basis set for all atoms, which is equipped with polarization functions for all atoms and diffuse functions for non-hydrogen atoms [58]. The electronic structure of multi-nuclear Fe–S clusters were composed from well-defined ionic fragments [57] with maximized number of anti-ferromagnetically coupled Fe ions [59,60] to obtain the lowest energy spin-coupling schemes in broken symmetry calculations for the thermodynamic analysis.

The greatest modeling challenge in describing aqueous equilibrium solutions is the capture of solvation effects. For the long-range electrostatic interactions, we selected the solvation model based on density (SMD) polarizable continuum model with the default water parameters [61]. The (aq) notation in the calculated species below implies the presence of only implicit continuum solvation, i.e., the presence of coordinately unsaturated Fe and S sites. However, for charged or significantly polarized species, we must include explicit solvent molecules to capture important H-bonding and coordinative bonding interactions that have significant covalent character, in addition to the ionic interactions represented by implicit solvation. In chemical reactions, when the bound solvent molecules were displaced from the inner coordination shell, we used rings of four to six water molecules: 4W, 5W, and 6W. Most of the structures presented here correspond to equilibrium stationary points without imaginary normal modes. Due to the flexibility of the inner sphere water molecules, some stationary structures could not be optimized to be free from imaginary frequencies that corresponded to water rotation without significantly impacting the structure of the solute molecules.

A highlight of our combined approach of reaction network modeling and density functional calculations is that we used the free energy values to generate equilibrium constants and enthalpy values to follow their temperature dependence. We constructed a reaction network for chemical equilibrium simulations that provides thermochemistry-based, mechanistic insights without explicit consideration of transition states. Towards this goal, we considered mostly elementary reaction steps that preferably excluded the presence of higher energy, unstable intermediates in contrast to combining several elementary steps into an overall stoichiometric reaction. Furthermore, the employment of 97 different functionals allowed us to evaluate the composition of the first solvation shell for experimentally characterized equilibria by tuning the number of water molecules, while minimizing the difference between the experimental and predicted log K values.

2.2. Equilibrium speciation modeling

The equilibrium aqueous speciation of iron and sulfur was calculated using PHREEQC v. 3 [62], iterating over solution compositions with PhreePlot v.1 [63]. Calculations used thermodynamic data from the MinteqA2 v. 4 database [64,65] distributed with PHREEQC v. 3 [62]. We reconciled iron (bi)sulfide stability constants with data reviewed by Rickard and Luther [66], following Johnson, Present, and Valentine [1]. Mackinawite was assumed to be the only mineral phase able to equilibrate with the solutions [1,7], with a solubility product constant defined by the reaction $FeS_{(m)}(s) + 2H^+(aq) \Leftrightarrow Fe^{2+}(aq) + H_2S(aq)$, $K_{sp1} = 10^{3.5}$ or $\Delta G^\circ = -20.0$ kJ/mol [67]. At neutral to alkaline conditions, mackinawite solubility is controlled by the presence of stacked two-dimensional Fe–S nanosheets of neutral charge with various degrees of intercalating water layers. These larger nanosheets are thermodynamically important, but their stoichiometry and speciation are experimentally ill-defined. We chose to model this indeterminate stoichiometry of $(FeS)_n(aq)$ with the reaction $Fe^{2+}(aq) + HS^-(aq) \Leftrightarrow (FeS)_n(aq) + H^+(aq)$,

$K = 10^{-2.2}$ or $\Delta G^\circ = +12.5$ kJ/mol, based on the intrinsic solubility of mackinawite in equilibrium with $(FeS)_n$ [67]. All calculations were performed under simplified model anoxic seawater conditions [1,7,68] with 2 mM Fe(II), pH 6.5, and 0.4 M NaCl unless otherwise noted.

Assembly and speciation of Fe–S clusters were modeled using the results of the DFT thermodynamic calculations (Appendix A). Several reaction schemes were possible, with different permutations of reactants, products, solvation states, and geometries. From the DFT results, we collated the energetically most stable compositions and geometries and formulated reactions as close to equimolar as possible to eliminate entropy driven or hindered reactions. There is a significant error in calculated translational entropy for solvated species [69], as the free volume for the solute is drastically reduced by the space taken up by solvent molecules compared to ideal gas phase conditions. Another important stoichiometry consideration (seen in Fig. 1) is the maximum number of Fe centers considered. To be able to compare the molecular cubane and nanosheet formations, we considered clusters up to cubanes and $(FeS)_4$(aq) species. The aqueous species $(FeS)_n$, $n > 4$, are represented in the reaction network by the "$(FeS)_n$(aq)" species.

3. Results

3.1. Accuracy of DFT models

It is commonly accepted that each density functional has its strengths and weaknesses in terms of chemical accuracy. The broad chemical space covered in this work includes ligand-metal complexation, limited solubility, acid/base chemistry, and redox chemistry. Thus, the use of a single functional will give results that are error prone. Hence, we chose a set of aqueous chemical equilibria as a training set to identify the best performing functionals for water autoionization ($\Delta G^\circ = 80$ kJ/mol), H_2S dissociation steps ($\Delta G_1^\circ = 40$ kJ/mol; $\Delta G_2^\circ = 106$ kJ/mol), coordinated water hydrolysis ($\Delta G^\circ_{Fe(II)} = 54$ kJ/mol; $\Delta G^\circ_{Fe(III)} = 12$ kJ/mol), $Fe(SH)^+$ formation ($\Delta G^\circ_{Fe(SH)+} = -25$ kJ/mol), and $(FeS)_n$(aq) acid dissociation ($\Delta G^\circ_{FeS} = 12.5$ kJ/mol). Two important points need to be made regarding these free energy values. The comparison of the water autoionization and second deprotonation of H_2S indicates that the formation of the sulfide anion is beyond water stability and it is an extrapolated value with significant uncertainty [22,70].

We assumed that the most plausible oxidizing agent for Fe–S clusters in aqueous solution is the hydronium ion, H_3O^+(aq). Therefore, the chemical accuracy of modeling with H_3O^+(aq) was assessed by estimating the water autoionization constant. The treatment of H_3O^+(aq)

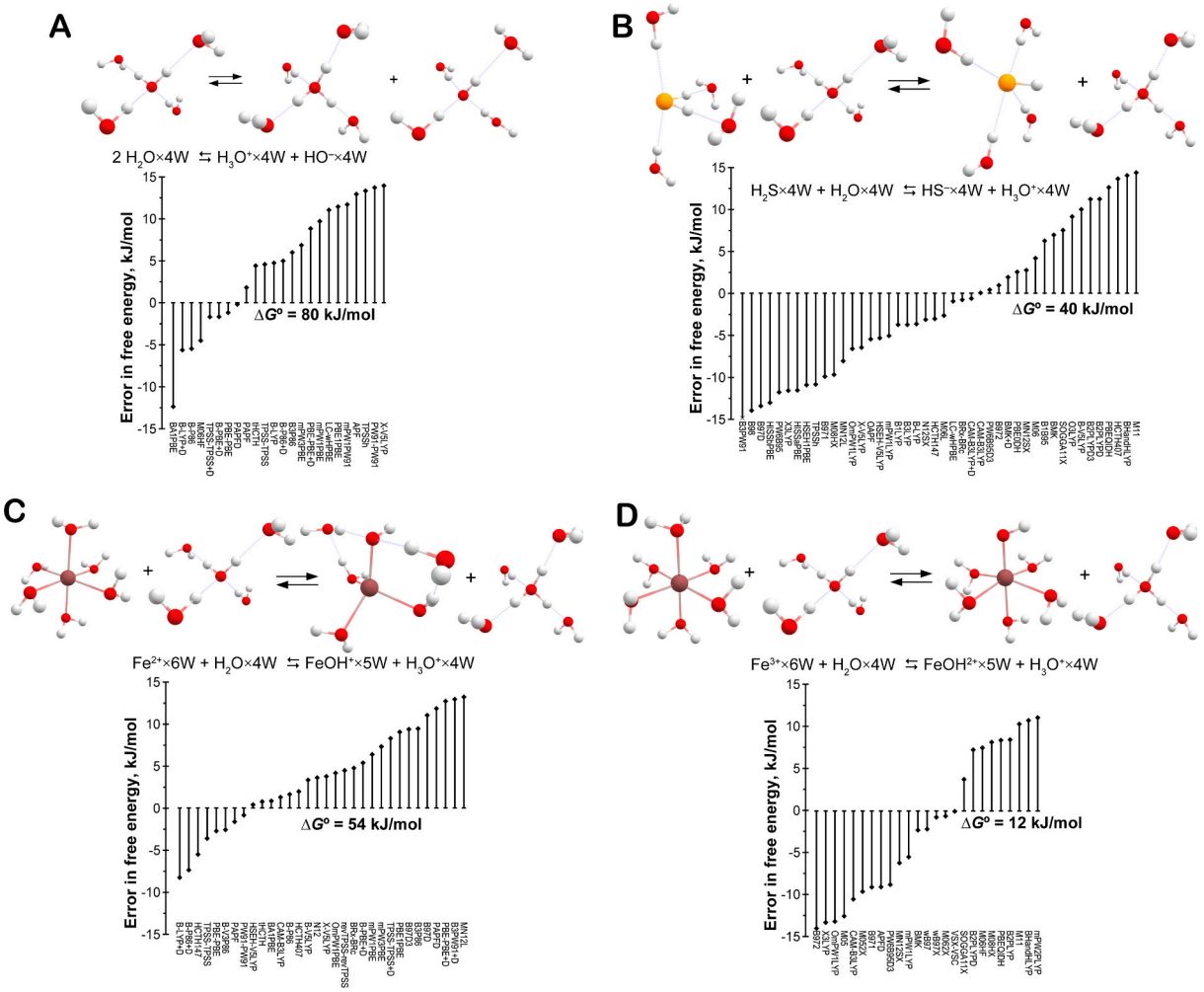

Fig. 2. Mapping of the error in estimating the free energy of reference reactions for top performing functionals within ±15 kJ/mol error using the def2TZVPPD basis set, SMD polarizable continuum, and explicit solvation. (A) Autoionization of water with tetrahedrally arranged solvent molecules (B) First proton dissociation of hydrogen sulfide using four explicit water solvent molecules in the inner sphere of S-species. (C) and (D) Errors in coordinated water ionization reactions at neutral pH using H_2O×4W as proton acceptor for ferrous (C) and ferric (D) hexaaquo complexes. Supplemental Material Fig. S1 provides the performance comparison of all 97 density functionals considered in the given study.

and HO^-(aq) requires the use of at least four explicit water molecules to capture the significant H-bonding donor and acceptor interactions, respectively. The top of Fig. 2A shows the explicitly solvated structures for the calculation of the free energy of dissociation. While the solvent cavity is not shown for the sake of clarity, implicit solvation by a polarizable continuum model was considered in all calculations. Below the molecular structure defined reactions in Fig. 2 are the graphical illustrations of the performance of the density functionals relative to the experimental values as given above.

First, we note that for the autoionization reaction (Fig. 2A), all functionals correctly predict the non-spontaneous nature of this equilibrium (Supplemental Material Fig. S1); however, the range of the free energies from 51 to 164 kJ/mol clearly justifies the need for the thermodynamic validation of the functionals owing to the approximate nature of these levels of theory. We can identify 13 functionals that reproduce the measured log K value within one unit that include APF+D [71], PBE [72], BLYP [73,74], TPSS+D [75,76], and tHCTC [77] functionals (Fig. 2A). Interestingly, the spectroscopically validated function for 4Fe–4S clusters, (B(5%HF)P86 functional [56,57]), reproduces the autoionization free energy within 5 kJ/mol; however, it fails to even qualitatively predict the non-spontaneity of ferric iron coordinated water ion hydrolysis (see below). Therefore, it was critical to expand the thermochemical validation of the functionals to additional relevant deprotonation, hydrolysis, and Fe–S complexation reactions.

The H_2S acid dissociation reactions are additional key equilibria required to describe the presence of the bisulfide ion and the formation of the iron coordinated sulfide as the nucleation step for Fe–S rhombs and cubanes. In addition, H_2S can be considered as a dual-function reagent because it can be the source of proton as electron acceptor, and a stabilizing ligand in concomitant coordination of HS^- to the oxidized Fe-species. By substituting the centrally located water molecule in Fig. 2A and generating the inner sphere solvation shell for H_2S(aq) and HS^-(aq), we can estimate the first log K value for $H_2S{\times}4W + H_2O{\times}4W \Leftrightarrow HS^-{\times}4W + H_3O^+{\times}4W$ equilibrium. As shown in Fig. 2B, there is a significantly wider range of functionals that reproduce the experimental value (40 kJ/mol) in comparison to the water autoionization. We can identify 26 functionals that reproduce the first pK_a value of 7.0 for H_2S (aq) within a log K unit, with some overlap with the above highlighted functionals.

The deprotonation equilibrium of HS^-(aq) to S^{2-}(aq) was a challenge to simulate. Using the same approach as for the first deprotonation step, there were only three functionals (HCTCH407 [75], M11L [78], and MN12L [78]) that approximated the experimental value of 106 kJ/mol within 10 kJ/mol. The average error for the calculated free energy and its standard deviation for the entire set of functionals were + 44 ± 13 kJ/mol, i.e., excessive overestimation of the free energy of reaction. The full equilibrium as considered for $HS^-{\times}4W + H_2O{\times}4W \Leftrightarrow S^{2-}{\times}4W + H_3O^+{\times}4W$ assumes a complete proton transfer and independent existence of a solvated sulfide, S^{2-}(aq) ion. This is not physically correct given that the $pK_{a,2}$ of H_2S is 4.5 units greater than pK_w. Therefore, we considered a model with only a proton transfer inside an explicitly solvated ion pair ($^-$S–H$\cdots$OH$^-$) to approximate the initial step of the formation of sulfide anion as shown in Fig. 3. The consideration of HO^-(aq) species as the proton acceptor is justified due to the physically realistic extreme alkaline conditions where S^{2-}(aq) may exist. The computations resulted in completely opposite, but still inaccurate trends, in which the average deviation changed to −65 ± 13 and − 65 ± 32 kJ/mol for the 7W and 8W models (Fig. 3), respectively; hence significantly underestimating the free energy of sulfide ion formation. The similar overall energetic differences independent of the number of inner sphere water solvent molecules allows us to conclude that neither the full dissociation nor the ion-paired models can describe accurately the sulfide formation equilibrium. An accurate description would likely require dynamic treatment with additional solvation shells, capturing resonance between sulfide-induced water ionization and proton abstraction from bisulfide by hydroxide. Due to this ill-defined stoichiometry, this equilibrium was not included in the training set to select the most reasonable level of theory for estimating the experimentally non-accessible log K values for Fe–S systems.

In turning to solvated iron cations, the first tests were of the deprotonation equilibrium of a coordinated water due to the Lewis acidity of the metal ion. The bottom sections of Fig. 2 summarize the top performing functionals for ferrous (C, exp.: 54 kJ/mol) and ferric (D, exp.: 12 kJ/mol) hydroxide complex formation at neutral pH. The first important difference from previously reported hydrolysis reactions [79] was that we located a more stable isomer for the ferrous hydroxide complex than the octahedrally coordinated Fe(II). The four-coordinate ferrous ion, with two water molecules solvating the covalently bonded HO^- ligand to the ferrous center, was found to be the lowest energy equilibrium structure. Although direct experimental validation of ferrous iron coordination geometries at variable pH remains challenging due to speciation changes, precipitate formation, and spectroscopic limitation, computational modeling studies indicate the decrease of iron coordination number as a function of the number of hydroxide ligands [80]. We found 17 functionals that reproduce the experimental log K value of −9.4 within one unit, including some functionals that have already been mentioned above, such as PBE, APF, tHTCT, and TPSS. The ferric hydroxide complex formation (Fig. 2D) showed a much more modest range of functionals accurate within one order of magnitude of the free energy.

The last two reference reactions for selecting the most reasonable functional focused on the binding of HS^-(aq) and S^{2-}(aq) ligands to Fe^{2+}(aq) ions. Similarly to the first ionization step of H_2S(aq), the description of the $Fe(SH)^+$(aq) species (Fig. 4A) was straightforward. Considering the $Fe^{2+}{\times}6W + HS^-{\times}4W \Leftrightarrow Fe(SH)^+{\times}5W + H_2O{\times}4W$ equilibrium, 17 density functionals reproduced the spontaneous reaction of −25 kJ/mol within a unit of log K value (4.3 ± 1). Using the 4W solvated bisulfide ion, the ligand exchange reaction results in a similar complex geometry to $[FeOH]^+$(aq) (Fig. 2C), in which solvent waters "bridge," via hydrogen bonding, the ligand and a water directly coordinated to the metal.

At neutral to alkaline pH, the intrinsic solubility of mackinawite mineral, $FeS_{(m)}$(s), is pH independent and represented by an equilibrium between the $FeS_{(m)}$(s) phase and the soluble nanosheets of $(FeS)_n$(aq) with a log K_{sp} of approximately −5.7 [67]. This non-spontaneous process ($\Delta G^\circ = +33$ kJ/mol) could not be reproduced by any of the functionals. This is an important result given that none of the levels of theory can approximate the experimental values without considering the

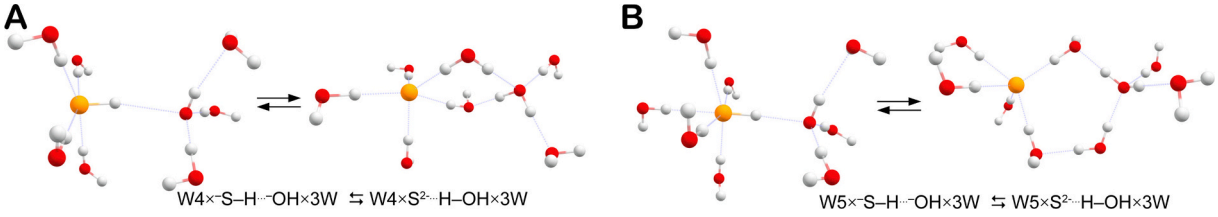

Fig. 3. Proton-transfer between HS^-(aq) and S^{2-}(aq) as an improved representation of equilibria for estimating the reaction thermodynamics of hydrogen sulfide dissociation using a single explicit solvation shell with 7 and 8 water molecules and assuming ion pairing.

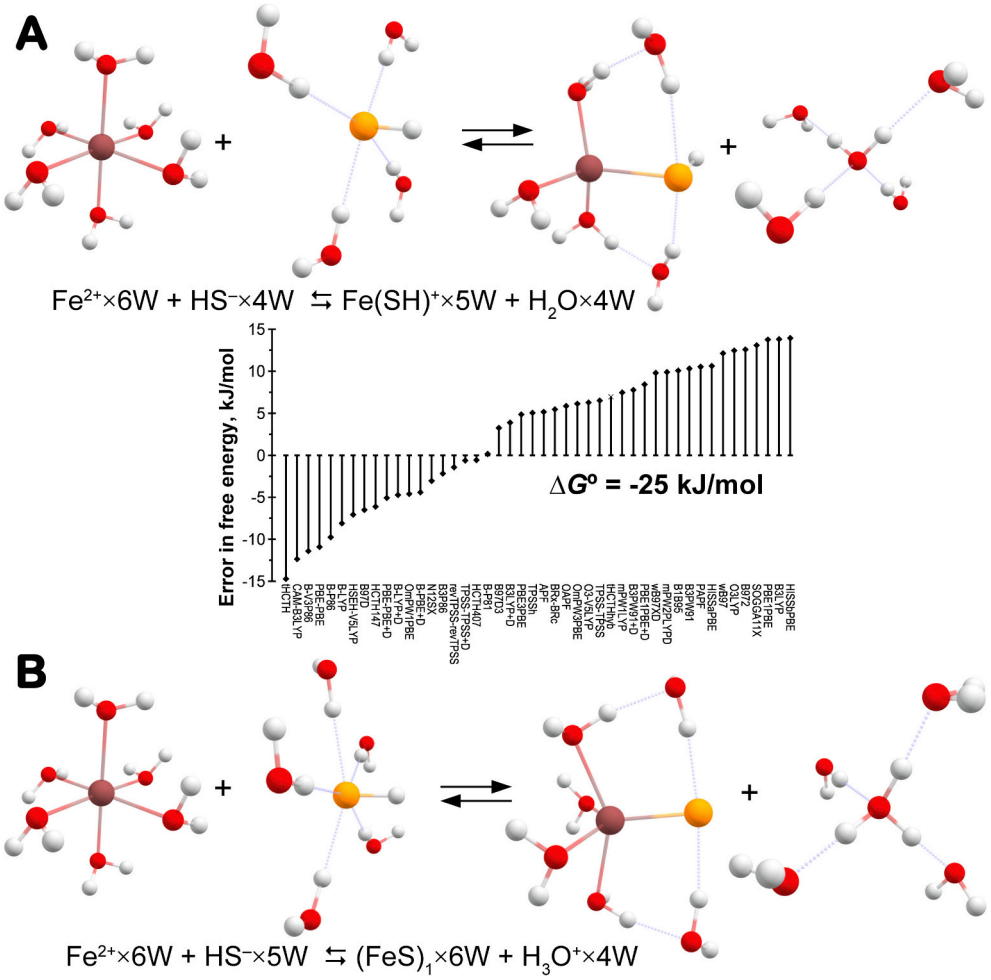

Fig. 4. Chemical reactions considered for the formation of (A) $Fe(SH)^{+}$(aq) and (B) $(FeS)_1$(aq) species using explicit solvation models. The errors are not shown for panel B due to the significant overestimation (average error of close to 100 kJ/mol) of the free energy change. The additional inner sphere water solvent molecule in $HS^{-}\times5W$ was required in B for achieving coordinatively saturated $(FeS)_1\times6W$ species.

speciation among various soluble $(FeS)_n$(aq) species, Fe^{2+}(aq), and HS^{-}(aq) ions. The complexation free energy for the $Fe^{2+}\times6W + HS^{-}\times5W \Leftrightarrow (FeS)_1\times6W + H_3O^{+}\times4W$ equilibrium was estimated to be 98 ± 19 kJ/mol for all the density functionals resulting in a penta-coordinate $(FeS)_1\times4W$ species with two additional water molecules solvating the sulfide ligand from the inner solvation shell (Fig. 4B). Alternatively, the deprotonation free energy of $Fe(SH)^{+}\times6W$ is estimated to be also strongly non-spontaneous with an enlarged standard deviation (97 ± 65 kJ/mol), when considering $H_2O\times4W$ to be the proton acceptor. Regardless whether we consider either the $FeS_{(m)}(s) + H^{+}(aq) \Leftrightarrow Fe^{2+}(aq) + HS^{-}(aq)$ or the $FeS_{(m)}(s) \Leftrightarrow (FeS)_n(aq)$ equilibria with $\Delta G^{\circ} = +12.5$ or + 32.5 kJ/mol, respectively, the error in the estimated equilibrium constant from a comprehensive set of density functionals can only be eliminated if we also consider the presence of a range of mackinawite-like $(FeS)_n$(aq) electroactive nanosheets.

In summary, we can tabulate the root mean square errors for the estimated equilibrium free energies obtained from 97 functionals for (i) water autoionization, (ii) first dissociation step of hydrogen sulfide, water ionization by (iii) ferrous and (iv) ferric ions, and (v) bisulfide complexation with ferrous iron. The common element for all reactions is the presence of solutes with compositionally well-defined inner-shell solvent environments. Table 1 presents the best performing functionals with the lowest RMS and average errors when employing def2TZVPPD basis set and SMD solvation model.

One of the insights from Table 1 is the limitation of density functional theory for reproducing the experimental equilibrium constants within a single unit of log K, since the top functionals show about 14 kJ/mol (or 3.3 kcal/mol) root mean square deviation in reaction free energy

Table 1
Top density functionals with the smallest root mean square and average errors (kJ/mol) calculated for deviation between experimental and calculated free energy values for reproducing water autoionization, hydrogen sulfide dissociation, proton dissociation from iron ligated water, and ferrous and bisulfide ion complexation.

Functional	Reference	RMS error	Average error
OmPW1PBE	[81]	13.8	−1.9
PBE0	[82]	14.2	1.2
APF	[71]	14.3	3.0
PBE3PBE	[83]	14.3	1.8
TPSS+D	[76]	15.0	−4.4
X3LYP	[81]	15.7	7.3
B3PW91 + D	[76,84]	16.5	2.8
HISSbPBE	[85]	16.5	5.8
revTPSS	[86]	16.9	−3.1
mPW1LYP	[81]	17.1	11.1
OmPW1LYP	[81]	17.5	10.4
B3P86	[84,87]	17.6	−5.9
wB97XD	[88]	17.7	5.5
TPSSh	[76]	17.8	0.4
OmPW3PBE	[81]	18.0	1.3
tHCTHhyb	[77]	18.4	3.3
HCTH147	[77]	19.0	−1.7

of the selected deprotonation and complexation reactions. Second, while some of the less commonly utilized functionals (OmPW1PBE, APF) lead the top of the list, methods with the Perdew-Burke-Ernzerhof functionals also show reasonable performances with average errors that are close to zero. In this paper, we are employing the top performing functional, OmPW1PBE, for calculating missing log K values for the Fe–S cluster formation and ligation equilibria with def2TZVPPD basis set and SMD polarizable continuum model. Interestingly, a closely related functional, mPW1B95, has been utilized in a recent and relevant study investigating the thermodynamic stability of prenucleation Fe–S clusters [89].

3.2. [4Fe–4S] and $(FeS)_4$ cluster assembly

We assembled the optimized geometries of a broad suite of reduced Fe(II) and reduced S(-II) species and complexes into a suite of equilibrium reactions using thermodynamic results from the OmPW1PBE/def2TZVPPD|SMD(water) level of theory. These reactions, summarized in the Appendix, demonstrate that key precursors to molecular [4Fe–4S] cubane clusters do not form spontaneously. For example, the deprotonation of $Fe(SH)^+$(aq) to the $(FeS)_1$(aq) monomer by H_2O is strongly non-spontaneous ($\Delta G^\circ = +103$ kJ/mol). However, other reactions, such as the oligomerization of $(FeS)_1$(aq), are strongly spontaneous ($\Delta G^\circ = -93$ kJ/mol). In Fig. 5, we represent a suite of reaction paths as a graph from Fe(II) and S(−II) to describe the competitive assembly of cubane $[4Fe–4S]^{0/+/2+}$ clusters and two-dimensional $(FeS)_4$(aq) sheets. Thermochemical data from the stationary DFT calculations are integrated into realistic aqueous chemical systems by using speciation modeling in the next section.

3.3. Stepwise assembly of Fe–S clusters and proton reduction

Starting from the Fe(II)(aq) and HS^-(aq) ions, we selected $(FeS)_1$(aq) to be the precursor molecule for Fe–S clusters that is formed by deprotonation of $Fe(SH)^+$(aq). The ionic interaction and the solvation energy of the ferrous bisulfide cationic species make the ion coupling spontaneous by −20 kJ/mol as a bisulfide ion displaces a Fe-coordinated water ligand (Fig. 4A) in the model reaction,

$$Fe(II) \times 6W + HS^- \times 4W \Leftrightarrow Fe(SH)^+ \times 5W + H_2O \times 4W.$$

The following step, deprotonation of $Fe(SH)^+$(aq), is significantly endergonic by 103 kJ/mol to reach the mononuclear $(FeS)_1$(aq) cluster precursor complex, as calculated using the OmPW1PBE functional. Given the importance of this deprotonation reaction to form the precursor to larger clusters, we also calculated the deprotonation of $Fe(SH)^+$(aq) with several other well-performing functionals from Table 1. Table 2 shows that the reaction remains reproducibly unfavorable regardless of the level of theory employed.

The deprotonation reaction is still slightly non-spontaneous (10 kJ/mol) when the presence of hydroxide is assumed at high pH condition,

$$Fe(SH)^+ \times 5W + HO^- \times 4W \Leftrightarrow (FeS)_1 \times 5W + H_2O \times 4W,$$

although the OmPW1PBE functional overestimates the acidity of water by 17 kJ/mol ($pK_w^{OmPW1PBE} = 17.1$).

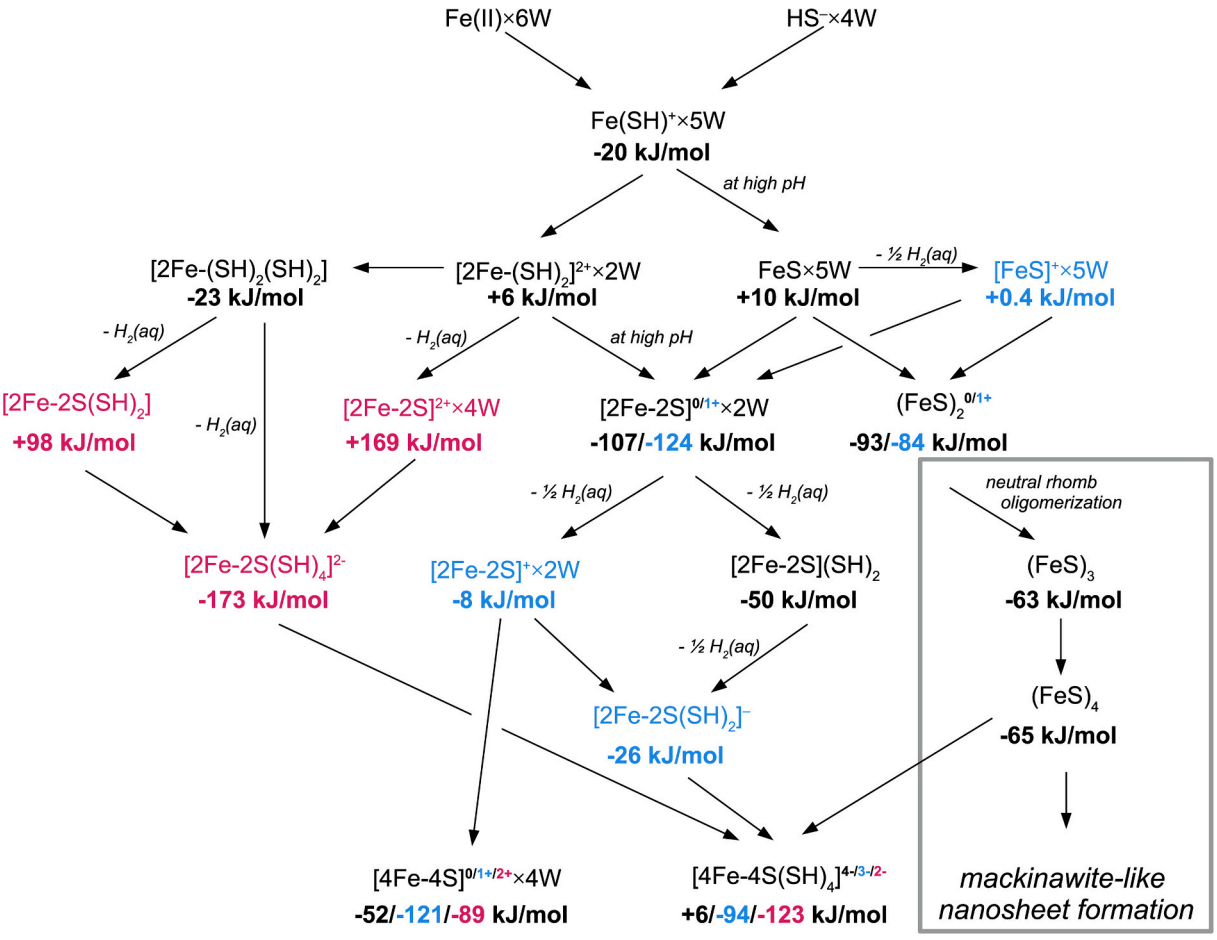

Fig. 5. Competitive pathways for the stepwise assembly of molecular rhombs and cubanes (left hand side) and mackinawite-like sheets (in the black box) from Fe(II) and HS^-. Gibbs free energy values are shown for the most favorable deprotonation, oxidation by proton, and ligand exchange reactions. Ferrous (black), single ferric (blue), and magenta (di-ferric) compositions are labeled by color coding. (For interpretation of the references to color in this figure legend, the reader is referred to the web version of this article.)

Table 2
Deprotonation reaction $Fe(SH)^{+}\times 5W + H_2O\times 4W \Leftrightarrow (FeS)_1\times 5W + H_3O^{+}\times 4W$ calculated with high-performing functionals from Table 1. In all calculations the def2TZVPPD basis was used and the SMD water solvation continuum.

Functional	ΔG° (kJ/mol)	ΔH° (kJ/mol)
OmPW1PBE	103	111
PBE1PBE	106	110
APF	107	109
TPSS+D	98	93
X3LYP	110	116
Average	*105*	*107*
Std. Dev.	*4.5*	*8.7*

Importantly, the oxidation of the $(FeS)_1$(aq) species by proton was estimated to be a near-equilibrium process ($\Delta G^{\circ} = 0.4$ kJ/mol) according to the reaction,

$$(FeS)_1 \times 5W + H_3O^{+} \times 4W \Leftrightarrow FeS^{+} \times 5W + H_2O \times 4W + \tfrac{1}{2}H_2(aq),$$

which is notably a non-equimolar reaction and hence there is uncertainty in the calculation of the entropic advantage of the right-hand side. The calculated free-energy change suggests that at standard conditions, approximately half of the $(FeS)_1$(aq) precursor species can be present in its oxidized form. However, at low pH, the acidic dissociation of FeS to HS^{-} or H_2S is far more favorable at −83 and − 105 kJ/mol, respectively:

$$(FeS)_1 \times 5W + H_3O^{+} \times 4W \Leftrightarrow Fe(II) \times 6W + HS^{-} \times 4W$$

$$(FeS)_1 \times 5W + 2\,H_3O^{+} \times 4W \Leftrightarrow Fe(II) \times 6W + H_2S \times 4W + H_2O \times 4W.$$

A thermodynamically much more favored reaction was identified that leads to cluster formation, taking the low concentration precursor molecule $(FeS)_1$(aq) towards oligomerization,

$$2\,(FeS)_1 \times 5\,W \Leftrightarrow [2Fe\text{–}2S](aq) \quad \text{or} \quad (FeS)_2(aq) + 2\,H_2O \times 4W,$$

with free energy change of −88 kJ/mol. The $n = 2$ member of the $(FeS)_n$(aq) series is special, given that both the Fe and S centers are only two coordinate. This renders the 2Fe rhomb as a starting point for both mackinawite-like 2D nanosheet and 3D cubane formation.

Coupling of two [2Fe–2S](aq) neutral rhombs to form a fully reduced, neutral [4Fe–4S](aq) cubane is non-spontaneous by 37 kJ/mol, which demonstrates the need of redox mediated cuboidal cluster formation. Oxidation of the [2Fe–2S](aq) rhomb by a proton are +8 and −8 kJ/mol in free energy for the two reactions below, when considering an uncoordinated rhomb [2Fe–2S](aq) and a rhomb with two inner-sphere solvent water molecules attached to the Fe sites [2Fe–2S]×2W, respectively:

$$[2Fe\text{–}2S] + H_3O^{+} \times 4W \Leftrightarrow [2Fe\text{–}2S]^{+} + H_2O \times 4W + \tfrac{1}{2}\,H_2.$$

$$[2Fe\text{–}2S] \times 2W + H_3O^{+} \times 4W \Leftrightarrow [2Fe\text{–}2S]^{+} \times 2W + H_2O \times 4W + \tfrac{1}{2}\,H_2.$$

The formation of biologically important 3D molecular clusters versus geological 2D nanosheets depends on the oligomerization pathway stemming from the $(FeS)_2$(aq) rhomb, which is influenced by whether coordinating ligands are present or absent. The less than two log units of difference between the two different solvated state of the [2Fe–2S](aq) or $(FeS)_2$(aq) cluster can be a critical point when the cluster growth pathways split among the mackinawite-like nanosheets, $(FeS)_n$(aq), $n <$ 150 or forming three-dimensional cubane structures, such as [4Fe–4S]. When no coordinating ligands are present, additional FeS(aq) precursor molecules can attach to the $(FeS)_2$(aq) cluster, and a sheet of Fe–S can be formed (highlighted with a box in Fig. 5). However, when coordinating ligands are present, the [2Fe–2S](aq) oxidation by proton will become favored, which then leads to coupling of the rhombs to form stable $[4Fe\text{–}4S]^{+/2+}$(aq) cubanes. The coordinating ligands, including weakly coordinating water molecules, can stabilize the oxidized cluster and promote accumulation of cubanes. The mixed valence rhomb $[2Fe\text{–}2S]^{+}$(aq) can further couple with either the neutral rhomb or with itself to give the one-electron reduced, paramagnetic S = 1/2, $[4Fe\text{–}4S]^{+}$(aq) cluster or the diamagnetic, resting form of $[4Fe\text{–}4S]^{2+}$ cluster of biological systems at −114 and −52 kJ/mol free energy change, respectively.

In addition to establishing that a proton can act as an oxidizing agent that facilitates cubane formation, we explored a parallel competitive process, which is the formation of higher nuclearity $(FeS)_n$(aq), $n < 150$ clusters that lead to the presence of electroactive nanosheet precursors to mackinawite. Taking [2Fe–2S] or $(FeS)_2$(aq) as the starting point, addition of another $(FeS)_1$(aq) precursor molecule to form the $(FeS)_3$(aq) and then $(FeS)_4$(aq) clusters (box in Fig. 5) is a strongly spontaneous process by −41 to −65 kJ/mol (depending on the arrangement of FeS units, Fig. 1), which is the thermodynamic signature for rapid oligomerization.

3.4. Coordinating ligands stabilize cubane structures

An important difference between biological Fe–S clusters and mackinawite-like nanosheets is the presence of terminal ligands, which prevent cluster oligomerization. Our second hypothesis is that when a ligand coordinatively saturates the Fe site, the three-dimensional molecular [4Fe–4S] cubanes become more stable than the two-dimensional nanosheets. To assess the validity of this hypothesis, we subjected the same set of 97 density functionals to cross evaluation of the relative stabilities of [4Fe–4S](aq) and $(FeS)_4$(aq) clusters in the presence of eight explicit water solvent molecules. Four of the water solvents were coordinatively bound to the redox active Fe centers, while four additional were H-bonding to the redox-active S ligands ([4Fe–4S]×8W vs. $(FeS)_4$×8W). Fig. 6 summarizes the molecular structures and their relative energies for the functionals shown in Table 1 with the lowest RMS error in reproducing the equilibria in the training set.

Most of the functionals plot in the top left highlighted area, including the best performing OmPW1PBE functional for proton dissociation and complexation (Table 1). This supports the hypothesis that, in the absence of coordinating ligands, the growth of the $(FeS)_n$(aq) mackinawite-like nanosheets will be thermodynamically favored over the formation of molecular cubane clusters owing to the stabilization of H-bonded solvent molecules and coordinating ligand. Water molecules will always be present in an aqueous solution; however, they can remain in the outer solvation shell of an analyte due to the entropic and enthalpic cost of desolvating the water from solvent bulk and bringing into the inner-sphere coordination environment as an explicit ligand. The spread of the thermochemically well-performing functionals in Fig. 6 is also cautionary with respect to the use of the validated level of theory. For OmPW1PBE (highlighted in red in Fig. 6), the solvated sheet $(FeS)_4$×8W is thermodynamically unfavorable (+30 kJ/mol), but the solvated cubane [4Fe–4S]×8W is strongly favored (−102 kJ/mol) as defined by $(FeS)_4$(aq) + 8W ⇔ $(FeS)_4$×8W zigzag isomer and [4Fe–4S](aq) + 8W ⇔ [4Fe–4S]×8W equilibria.

Notably, we utilized one of the least covalent ligands in Fig. 6, neutral water, which only weakly stabilizes the cubane clusters. However, ammonia, bicarbonate, chloride, bisulfide, thiolate, and similarly stronger Lewis bases can further stabilize the three-dimensional cluster structures over the two-dimensional sheets. To test this, we considered the coordination of HS^{-}, as the smallest mimic of the biologically important cysteine thiolate side chains. Bisulfide can directly coordinate the [2Fe–2S] rhombs and [4Fe–4S] cubanes, as shown in the central path of Fig. 5. Indeed, the DFT calculations show that bisulfide-coordinated rhombs and cubanes are more stable than the water coordinated forms by −27 kJ/mol:

$$[2Fe\text{–}2S] \times 2W + 2\,HS^{-} \times 4W \Leftrightarrow \left[2Fe\text{–}2S(SH)_2\right]^{2-} + 2\,5W.$$

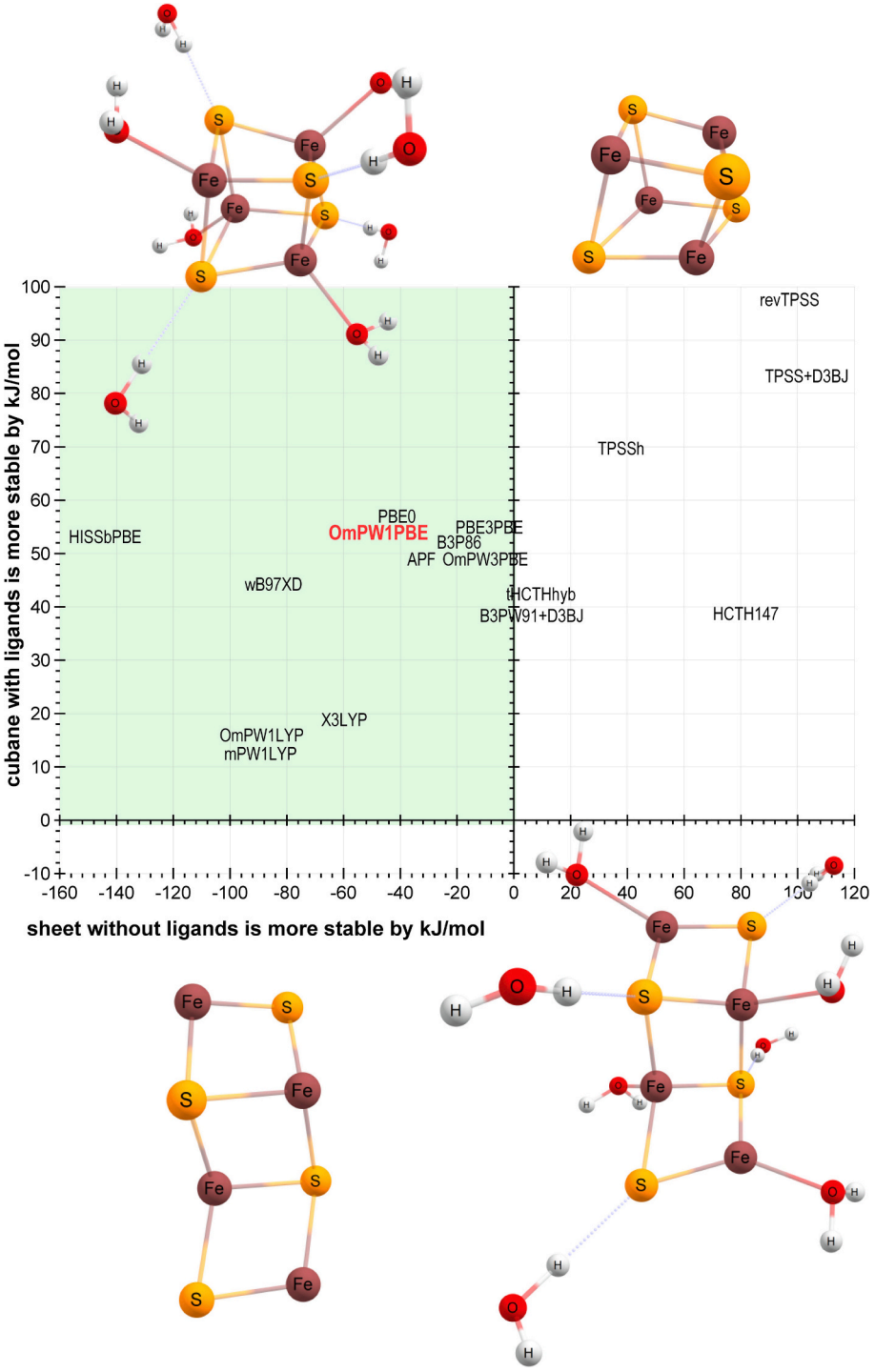

Fig. 6. Relative stability (ΔG°) of the linear $(FeS)_4$(aq) isomer (bottom left inset) and the [4Fe–4S](aq) cubane (upper right inset) and their explicitly solvated models ([4Fe–4S]×8W in upper left and $(FeS)_4$×8W bottom right corners) embedded into the SMD water polarizable continuum using def2TZVPPD basis set for the thermochemically validated functionals from Table 1.

The oxidized, cationic species are even more favored (−45 kJ/mol) to complex with HS^-:

$$[2Fe\text{–}2S]^{+} \times 2W + 2\ HS^{-} \times 4W \Leftrightarrow [2Fe\text{–}2S(SH)_2]^{-} + 2\ 5W.$$

Ultimately, the oxidized, bisulfide-coordinated rhombs are also strongly favored to oligomerize (−94 and −123 kJ/mol) and form cubanes, but this is not true for the all-ferrous rhomb and cubane (+6 kJ/mol):

$$2\ [2Fe\text{–}2S(SH)_2]^{2-} \Leftrightarrow [4Fe\text{–}4S(SH)_4]^{4-}$$

$$[2Fe\text{–}2S(SH)_2]^{2-} + [2Fe\text{–}2S(SH)_2]^{-} \Leftrightarrow [4Fe\text{–}4S(SH)_4]^{3-}$$

$$2\ [2Fe\text{–}2S(SH)_2]^{-} \Leftrightarrow [4Fe\text{–}4S(SH)_4]^{2-}.$$

3.5. Dimerization of $Fe(SH)^+$

Bisulfide as a coordinating ligand further affects cluster formation by stabilizing key intermediates. The covalent Fe–SH bond, even in the cationic species, significantly reduces the electrophilicity of the metal center and shifts part of the electron holes from the metal to the ligand. In addition, the SH^- ligands can act as a proton source for S-based redox chemistry and inner-sphere evolution of H_2 while the FeS unit becomes oxidized. To map out this reaction path (along the left-side branches in Fig. 5), the dimerization of $Fe(SH)^+$ was considered. At OmPW1PBE level, this is a near-equilibrium process (+6 kJ/mol) at standard conditions:

$$2\ Fe(SH)^+ \times 5W \Leftrightarrow [2Fe\text{–}2(SH)]^{2+} \times 2W + 2\ 4W.$$

The formation of this $Fe(SH)^+$ dimer may be followed by the strongly exothermic (−125 kJ/mol) deprotonation of the dimer, forming a neutral [2Fe–2S] rhomb:

$$[2Fe\text{–}2(SH)]^{2+} \times 2W + HO^- \times 4W \Leftrightarrow [2Fe\text{–}2S] \times 2W + 2\ H_2O \times 4W.$$

Alternatively, the protonated dimer could dehydrogenate, resulting in a super-oxidized $[2Fe\text{–}2S]^{2+}$ rhomb, but this species is extremely unfavorable thermodynamically (+169 kJ/mol), due to the too low oxidation potentials for the simultaneous two electron coupling with two protons at the sulfide ligands:

$$[2Fe\text{–}2(SH)]^{2+} \times 2\ W \Leftrightarrow [2Fe\text{–}2S]^{2+} \times 2\ W + H_2.$$

In order to lower the oxidation potential, the water and bisulfide ligands can exchange by the reaction,

$$[2Fe\text{–}2(SH)]^{2+} \times 2W + 2HS^- \times 4W \Leftrightarrow [2Fe\text{–}2(SH)](SH)_2 + 6W,$$

which increases the electron density on the cationic $[2Fe\text{–}2(SH)]^{2+}$ dimer and was calculated to be favorable at −23 kJ/mol. In the neutral $[2Fe\text{–}2(SH)(SH)_2]$ cluster, the inner-sphere H_2 evolution reaction becomes significantly less endergonic (+98 kJ/mol), which prompted us to consider the formation of a double oxidized rhomb with a fully saturated coordination environment,

$$[2Fe\text{–}2(SH)(SH)_2] + 2\ HS^- \times 4W \Leftrightarrow [2Fe\text{–}2(SH)(SH)_4]^{2-} + H_2 \times 2W + 6W.$$

The resultant $[2Fe\text{–}2(SH)(SH)_4]^{2-}$ species now affords for the spontaneous (−27 kJ/mol) formation of the 2-electron oxidized rhomb. The explicitly solvated $H_2{\times}2W$ species maintains equimolar reaction. Notably, this particular charge state for the [2Fe–2S] rhomb, but with cysteine-derived thiolate coordination, is the resting form of plant ferredoxins. The coordinatively saturated, negatively charged all-ferric rhomb opens access to all biologically relevant oxidation states of [4Fe–4S] cubanes by H_2 evolution via intramolecular electron-transfer and formation of oxidized [2Fe–2S] building blocks for higher nuclearity clusters.

3.6. Oxidation by H_2S

Given the favorable oxidation of $[2Fe\text{–}2S]^0$(aq) rhombs by proton and the stabilizing effect of HS^-(aq) on the formally Fe(III) ion containing rhombs, we also considered the combined oxidation and ligation by H_2S(aq). Solely the oxidation from an H_2S derived proton, i.e.,

$$[2Fe\text{–}2S] + 2\ H_2S \times 4W + 4W \Leftrightarrow [2Fe\text{–}2S]^{2+} \times 4W + 2\ HS^- \times 4W + H_2,$$

is unfavorable at standard conditions by +93 kJ/mol. If the protons dehydrogenate *and* the bisulfides remain in the inner sphere to coordinate and stabilize the product, the reaction,

$$[2Fe\text{–}2S] + 2\ H_2S \times 4W \Leftrightarrow [2Fe\text{–}2S(SH)_2] + H_2 + 2\ 4W,$$

is closer to equilibrium, but still non-spontaneous ($\Delta G^\circ = +13$ kJ/mol). Near pH values of the first pK_a of H_2S(aq), both H_2S(aq) and HS^-(aq) are measurably significant species, suggesting that the combined ligation and oxidation can be very favorable ($\Delta G^\circ = -112$ kJ/mol):

$$[2Fe\text{–}2S] + 2\ H_2S \times 4W + 2\ HS^- \times 4W \Leftrightarrow [2Fe\text{–}2S(SH)_4]^{2-} + H_2 + 4\ 4W.$$

However, this favorable free energy value for simultaneous proton reduction and bisulfide ligand coordination is calculated for a non-elementary reaction step, where the three reactants must undergo considerable coordination sphere reorganization work while forming energetically less-favorable intermediates *en route* to the coordinatively-saturated rhomb. The consequences of combining multiple elementary steps in the equilibrium speciation modeling and abandoning the mechanistic details as shown above for the neutral rhomb oxidation by H_2S reaction are further elaborated in the Supplemental Material.

3.7. Equilibrium speciation of clusters

Several pathways from aqueous Fe(II) and HS^- precursors to Fe–S clusters appear to be thermodynamically feasible. By modeling the reaction network in Fig. 5 with PHREEQC, we explored the speciation of clusters and intermediates in model seawater with 2 mM Fe(II) concentration under anoxic conditions at low sulfur (30 μM sulfide) levels and with salinity similar to modern oceans (0.4 M NaCl).

The speciation of aqueous Fe and S is pH dependent (Fig. 7A). At low pH (<5), most dissolved sulfide exists as H_2S(aq) and is not complexed to iron. While $Fe(HS)^+$ does form, it remains protonated. Deprotonation of $Fe(HS)^+$ to FeS(aq) is more favorable at alkaline pH (>8), but polymerization into FeS_n(aq) nanosheets at high pH is so strongly favored that molecular cubanes cannot accumulate; nearly all sulfide is funneled towards mackinawite precipitation. At circumneutral pH (~6–7), bisulfide is available for complexation and proton activity is sufficient to drive oxidation of rhombs and cubanes, enabling a competing pathway to molecular cluster formation. At this pH, $Fe(HS)^+$ forms readily and can dimerize to $[2Fe\text{–}2(SH)]^{2+}$ with the proton remaining in the inner coordination sphere. Coordination by additional bisulfide ligands enables dehydrogenation to $[2Fe\text{–}2S(SH)_4]^{2-}$ with H_2 release.

This circumneutral pH provides a thermodynamic path towards cubane formation and coincides with estimated Archean seawater pH [68]. At 6.5 pH, mackinawite has precipitated, leaving only 7.4 μM total aqueous sulfide in solution. Of the remaining aqueous sulfide that is complexed to iron, most (1.7 μM) is speciated as indeterminate neutral $(FeS)_n$(aq), $4 < n < 150$, clusters denoted "$(FeS)_n$(aq)" in Fig. 7 (the exact stoichiometries of these larger species are unknown). The solution also contains 423 nM $Fe(SH)^+$. However, the solution contains only tiny amounts, 8 pM, each, of $[2Fe\text{–}2S]^0$ and $[2Fe\text{–}2S]^+$ water coordinated rhombs. The oxidized $[4Fe\text{–}4S]^{2+}$ water-coordinated cubane dominates total cubane concentrations at 3.4 pM. Other sulfur species, such as coordinatively unsaturated clusters of various stoichiometries, the $(FeS)_1$(aq) monomer precursor, and bisulfide dimers, are calculated to be effectively non-existent at sub pico- to femtomolar concentrations, indicating that their clustering towards the larger $(FeS)_n$(aq), $4 < n < 150$, nanosheets (which are not explicitly modeled with DFT calculations) is heavily preferred.

The thermodynamic importance of these large $(FeS)_n$(aq) clusters is apparent in Fig. 7B, in which mackinawite mineral precipitation has been manually suppressed. At all alkaline pH compositions, these large clusters dominate the total dissolved sulfide pool. This version of our reaction network provides a snapshot of the chemical speciation during the early stages of cluster formation and shows the aqueous species that are metastable with respect to mackinawite. Notably, at circumneutral

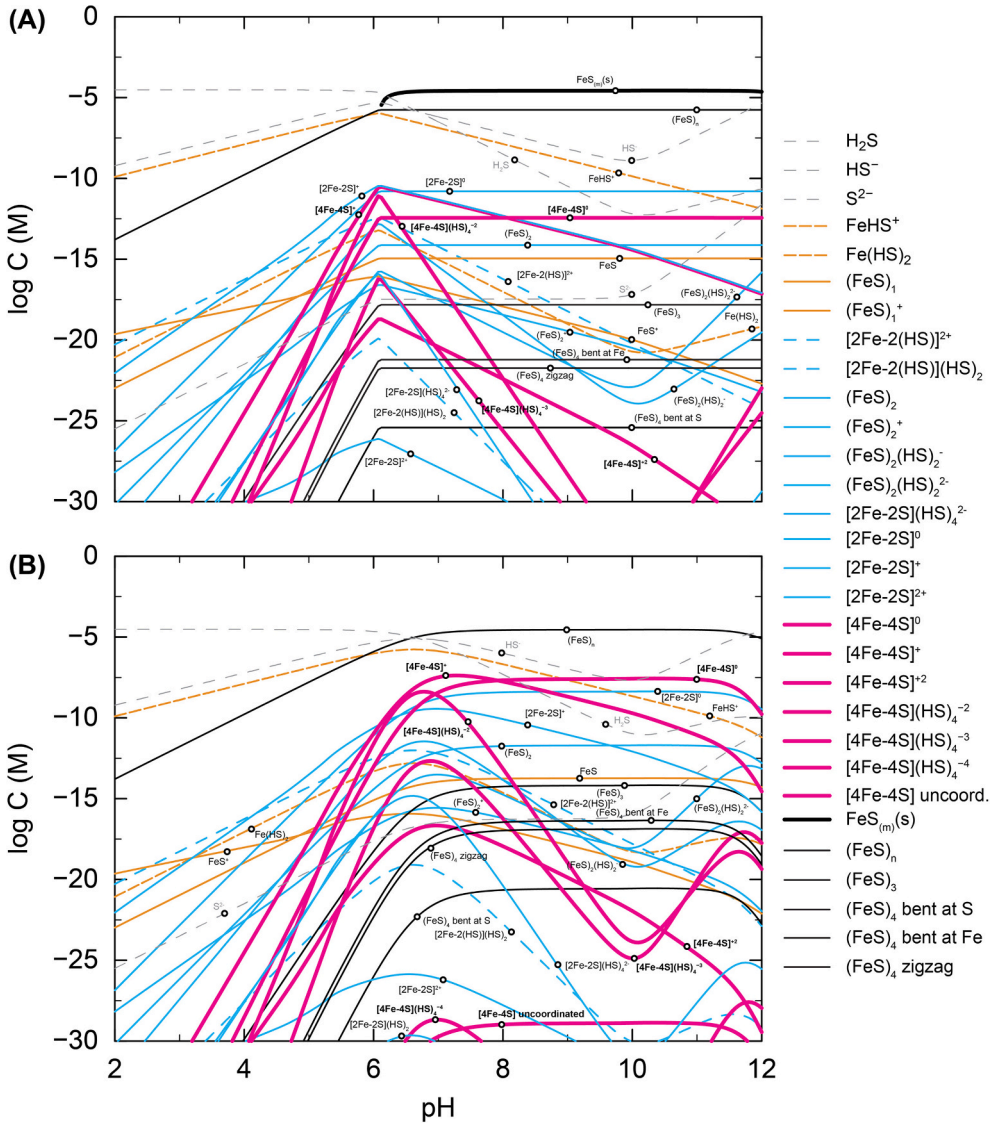

Fig. 7. Speciation of S in model ferruginous seawater (30 μM S(-II), 2 mM Fe(II), 0.4 M NaCl). (A) Speciation in equilibrium with mackinawite mineral, denoted $FeS_{(m)}(s)$. (B) Speciation with mackinawite precipitation suppressed.

pH, nanomolar concentrations of bisulfide-coordinated [4Fe–4S] cubanes form in equilibrium with the $(FeS)_n(aq)$, $4 < n < 150$, nanosheets when mackinawite precipitation is suppressed.

The important roles for HS^- complexation and coordination are seen in the predominant sulfur species at different total sulfide concentrations (Fig. 8). Fig. 8B is calculated without permitting $(FeS)_n(aq)$ to precipitate as $FeS_{(m)}(s)$, and so the total sulfide activities are unrealistically high. (Thermodynamically more stable iron sulfide minerals, such as greigite or pyrite, are stable across a wide range of solution compositions; however, they tend to require the precipitation of mackinawite or other precursors [46,90] due to limiting reaction mechanisms and kinetics). These high bisulfide concentrations support bisulfide-coordinated $[4Fe–4S]^{2+}$ clusters near circumneutral pH and total sulfide concentrations on the order of 100 μM, where the hydronium activity and bisulfide activity are both high enough to oxidize and stabilize the clusters. At lower total sulfide, $H_2S(aq)$, $HS^-(aq)$, and large $(FeS)_n$ polymers predominate.

The Supplemental Material further shows the thermodynamic importance of bisulfide coordination when combined with proton oxidation via the H_2S-mediated oxidation pathway. When $H_2S(aq)$ is the species that brings both a proton and bisulfide ligands to interact with the neutral [2Fe–2S] rhomb, the resultant $[2Fe–2S(SH)_4]^{2-}$ oxidized species forms readily at circumneutral pH (Supplemental Material Fig. S2). We estimate that this plant ferredoxin-like inorganic species could predominate at order 100 μM sulfide concentrations and higher (Supplemental Material Fig. S3). Although this species is extremely stable across a wide range of conditions, the description of this process with a single reaction from combined elementary steps neglects the importance of unstable cationic intermediates, such as $[2Fe–2S(SH)_2]^{2+}$, which do not form spontaneously by the dehydrogenation of the $Fe(HS)^+$ dimer or the proton-assisted oxidation of $[2Fe–2S]^0$ rhomb/$(FeS)_2$ species.

4. Discussion

4.1. Equilibrium concentration of a Fe–S cluster precursor

In Archean oceans, geologic evidence indicates that Fe(II) concentrations exceeded total sulfide by orders of magnitude, so iron controlled the aqueous speciation of sulfide [1,7]. Mackinawite solubility set the maximum concentrations of Fe(II) and S(−II) species, including Fe–S clusters. However, the identity, stability, and formation pathways of the aqueous precursors to molecular Fe–S clusters are poorly understood to date.

At issue is the fundamental assembly of an aqueous complex between

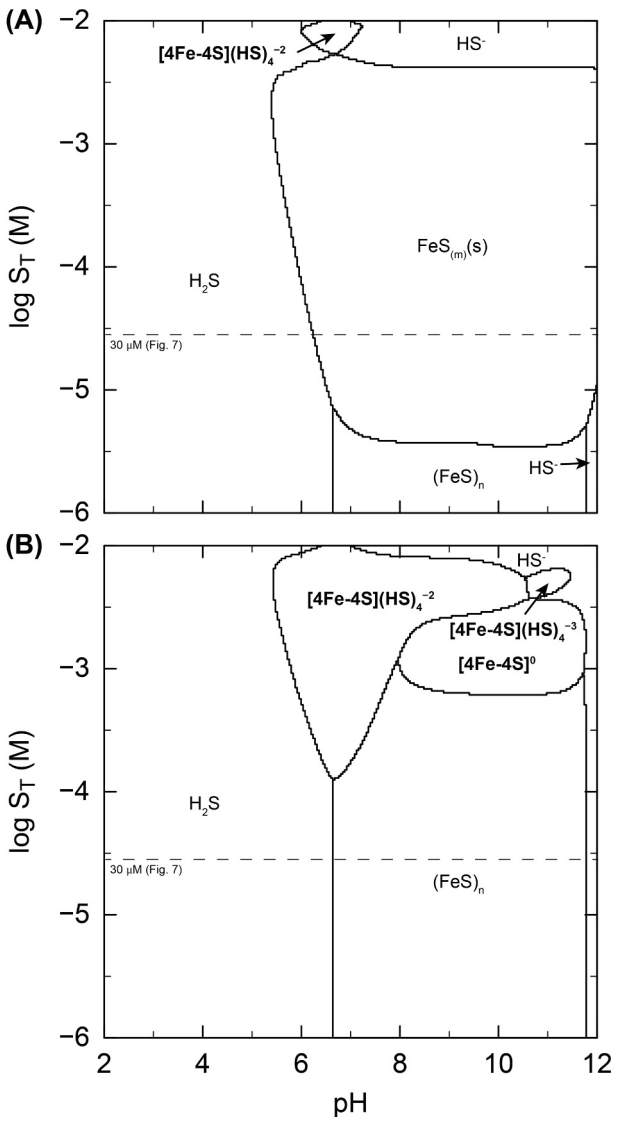

Fig. 8. Predominant S species in model ferruginous seawater (2 mmol/kg Fe(II), 0.4 M NaCl). (A) Predominant species including mackinawite precipitates. (B) Predominant species when mackinawite is suppressed from precipitating when saturated.

Fe(II) and HS^-. Experimental estimates for the $Fe(SH)^+$ binding constant vary between log K of 1.4 to 6, with several experimental estimates centering around 5.2, though some works have suggested that its value is approximately 2 orders of magnitude lower [22,66,91]. Rickard [67] showed how nanoparticulate FeS(s), likely a mackinawite-like phase, is at equilibrium with both Fe^{2+}(aq) and $(FeS)_n$(aq) species (with indeterminate *n*), but his solubility data was inconsistent with appreciable concentrations of iron-bisulfide polymers. The solubility data showed an increasing importance of $(FeS)_n$(aq) species with pH [92]. Similarly, Davison et al. [93] argued for no evidence of $Fe(SH)^+$ species, but explained amorphous FeS(s) solubility with predominately free Fe^{2+}(aq) and subordinate polymeric bisulfide $Fe_n(HS)^0_{2n}$(aq) species (also with indeterminate *n*). Rickard considers these bisulfide species to be metastable intermediates that decompose to FeS monomers or polymers [22,67,94]. Complicating estimates of aqueous Fe speciation from solubility measurements, Wolthers et al. [95] show how nanoparticulate mackinawite is a disordered mixture of at least two phases, whose solubility and reactivity thus depends on their ordering, structural water, and crystallinity. Kinetic data for $FeS_{(m)}$(s) precipitation under low total sulfide conditions shows that precipitation predominately occurs by direct sulfidation of Fe(II) by H_2S(aq) rather than via iron bisulfide intermediates [94].

Our thermodynamically validated calculations using the OmPW1PBE functional provide insight into this complex speciation landscape, albeit with approximately 14 kJ/mol of uncertainty (Table 1). The calculated $Fe(SH)^+$ binding constant (log K = 3.5) falls within the experimental range and closer to the lower estimates [22,66,89,91]. Critically, our calculations predict strongly positive free energy values for the deprotonation of $Fe(SH)^+$ to form mononuclear $(FeS)_1$(aq). For example, the deprotonation of $Fe(SH)^+$ by OH^- has a calculated pK_{eq} value of 1.8, indicating that less than 2% of the total iron complexed by sulfide would be deprotonated at standard conditions, and much lower at higher pH. Formation of the neutral species $Fe(SH)^0_2$(aq) is similarly unfavorable ($\Delta G^\circ = +10$ kJ/mol), consistent with their metastable status with respect to larger clusters [22,67,94]. Moreover, direct production of a $(FeS)_1$(aq) monomer from either HS^- or H_2S is extremely unfavorable.

Despite its non-spontaneous formation from $Fe(SH)^+$ deprotonation, the $(FeS)_1$(aq) monomer is important, serving as the precursor for far more favorable polymerization and oxidation reactions. The modeling of the full reaction network shows that the $(FeS)_1$(aq) monomer might exist at very low concentrations in equilibrium with larger clusters (Fig. 7). However, to be consistent with the solubility of $FeS_{(m)}$(s), the total concentration of neutral $(FeS)_n$(aq) species with 1Fe:1S stoichiometry with $n \leq 4$ must be a small fraction of the total nanoparticle or cluster concentration, and the exact stoichiometries of the larger species are unknown.

4.2. Environmental stability of [4Fe–4S] cubanes

Aqueous iron sulfide species limit the maximum total iron concentration in Precambrian seawaters and control the proportion of this iron that is readily available to life as "free" Fe^{2+}-*aquo* complexes [1,7]. Under Earth's earliest ferruginous conditions, low sulfide concentrations supported high free Fe^{2+} concentrations for wide use in rubredoxin-like, mononuclear proto-metalloenzymes and other enzymatic functions [1]. But, to access the chemical capabilities of ferredoxin-like enzymes with Fe–S clusters, most authors have suggested that life orchestrated a way to obtain or assemble specific low-*n* polymers of $(FeS)_n$(aq) [17,25,34,96].

To date, cubane $[4Fe–4S]^{2+}$ clusters have only been synthesized in vitro from Fe(III), typically in the excess of coordinating ligands and reductants [25,27,34–36,97,98]. Therefore, Earth's strongly reducing surface during the emergence and early evolution of life, with limited Fe(III), was an existential challenge given the important roles these clusters presumably played in earliest life's metabolisms. Some environments, like shallow, UV light-irradiated ferruginous seas, may have accumulated enough Fe(III) to support cluster assembly [34]. In addition, alkaline lakes may have contained many of the essential prerequisites for metalloprotein precursors [97–100], but [4Fe–4S] cubane clusters may not predominate under such conditions [35]. Environments with steep chemical potential gradients, such as alkaline or off-axis hydrothermal systems venting sulfidic fluids into more acidic seawater, also may have supported local enrichments of both Fe–S clusters and iron sulfide minerals [16,25]. Nonetheless, even if life first evolved using clusters in specific, limited environments like these, it clearly diversified broadly across the reducing ocean and sediments blanketing Earth. The central question of our study is whether the rhomb and cubane cofactors of proto-ferredoxins could have formed at biologically significant (e.g., micromolar) concentrations in deep oceans and sediments that lacked Fe(III).

The DFT calculations here show there may be additional paths towards cubane assembly and oxidation, which might expand the range of plausible environments where early life could begin to interact with them. Although proton oxidation of the FeS monomer is unfavorable at circumneutral pH, coupling of the oxidized FeS^+(aq) monomer into

rhombs and cubanes, as well as proton oxidation of rhombs and cubanes themselves, is highly favorable. In addition, while dimerization of $Fe(HS)^+$ is a near-equilibrium process, oxidation by the inner-sphere proton to form H_2 and the oxidized, di-ferric rhomb is highly favorable. The protonated rhombs can be further stabilized when nucleophilic ligands like HS^- bind to the coordinatively unsaturated Fe sites or displace ligated water molecules. Together, modeling of the complete reaction network shows that picomolar concentrations of cubanes can accumulate in equilibrium with mackinawite at mildly acidic to neutral conditions (Fig. 7).

Despite analytical challenges in characterizing clusters [101–103], available experimental observations are broadly consistent with our calculated thermodynamic predominancies. Under alkaline conditions (pH 9 to 11), Jordan et al. [25] showed that cysteine and bicarbonate stabilize cubane clusters formed from Fe(III), but only mononuclear complexes and $[2Fe–2S]^0$ rhombs formed from pure Fe(II). Scintilla et al. [97] reduced Fe(III) with glutathione at pH 8.6, and demonstrated that increasing HS^- concentrations promoted [4Fe–4S] cubane stabilization. Ivernici et al. [40] showed that excess sulfide with respect to Fe results in the dominance of [4Fe-4S] cubanes over rhombs. Sanden et al. [96] co-synthesized [4Fe–4S] clusters from Fe(III) in the presence of a tetrathiolate chelating peptide, demonstrating a stabilizing role of multidentate ligands.

A fundamental bifurcation in the assembly pathways determines whether iron and sulfur ions form geologically sequestered nanoparticles or minerals or accumulate biologically relevant molecular clusters. A trivial route to cubanes proceeds through the FeS monomer, but, as described above, its formation by deprotonation of $Fe(HS)^+$ is highly unfavorable. At alkaline pH, what little FeS(aq) forms polymerizes rapidly, resulting in the dominance of the $(FeS)_n$(aq) nanosheets. An alternative pathway bypasses the bottleneck created by the high pK_a of $Fe(HS)^+$. $Fe(HS)^+$ can dimerize directly, retaining the proton in the inner coordination sphere. Bisulfide then serves several important roles: stabilizing the three-dimensional cluster geometry, saturating the metal center and preventing nanosheet polymerization, and delivering the inner-sphere proton that can act as electron-acceptor in order to form the oxidized [2Fe–2S] cluster.

The importance of coordinating ligands on cluster stabilization is seen in Fig. 6. Using water as a minimal coordinating ligand, we compared the relative stabilities of naked $(FeS)_4$(aq) nanosheets versus [4Fe–4S](aq) cubanes and their water-coordinated forms. Without coordinating ligands, the naked $(FeS)_4$(aq) nanosheet is favored; with inner-sphere water coordination, the [4Fe–4S]x4W cubane becomes more stabilized. Water is among the weakest coordinating ligands; bisulfide, thiolates, and chelating short peptides (as bioligands) are expected to enhance this effect substantially. Thus, the presence of any coordinating ligand at the critical [2Fe–2S] rhomb stage can redirect cluster assembly from the nanosheet pathway towards molecular cubanes.

Fig. 8 illustrates this bifurcation under Archean ocean conditions. The upper panel (Fig. 8A), which includes equilibrium with mackinawite mineral precipitation, shows that sulfur at circumneutral conditions is predominantly either mackinawite precipitate or its aqueous precursor: the large $(FeS)_n$ nanosheets. The mackinawite mineral also buffers total sulfide to micromolar concentrations, holding molecular cubane concentrations to exceedingly low picomolar concentrations (Fig. 7A)—likely far too low to support meaningful interaction with primitive bioligands. However, suppressing mackinawite precipitation (Fig. 8B) reveals the aqueous equilibrium sulfur speciation under highly supersaturated conditions. The latter model can be relevant when considering the initial phases of Fe–S cluster formation at low nuclearity. At elevated total sulfide (~100 μM), bisulfide-coordinated $[4Fe–4S]^{2+}$ cubanes become the predominant sulfide species at circumneutral pH. This occurs because both hydronium and bisulfide activities are sufficiently high: hydronium provides the oxidizing equivalents necessary to form the cationic cluster and its precursors, while bisulfide coordination stabilizes the oxidized, three-dimensional cubane geometry against forming 2D nanosheets. Critically, this coordination prevents the clusters from polymerizing into the $(FeS)_n$(aq) species that control mackinawite solubility.

Admittedly, achieving the favorable stabilizing bisulfide concentrations while preventing mackinawite precipitation violates the fundamental thermodynamic control on the system. At low sulfide concentrations, the system follows the thermodynamically favorable path towards $(FeS)_n$(aq) nanoparticle and mackinawite mineral phases. At high sulfide concentrations with lower Fe:S ratio than in bulk Archean seawater, bisulfide-stabilized molecular cubane clusters can predominate, but they remain only metastable with respect to mackinawite in natural systems. High sulfide conditions may have existed near low-temperature hydrothermal vents during Hadean or Archean time [15,16,97,98]. Elsewhere, to access the key ferredoxin cofactors [2Fe–2S] and [4Fe–4S] species, life or its environment needed to prevent the accumulation of large $(FeS)_n$(aq) nanosheets and mineral precipitates.

4.3. Fe–S cluster bio-obtainability

For early life to use Fe–S clusters enough to evolve dependence on their chemical capabilities and thus later evolve sophisticated acquisition and management pathways, it first needed to encounter them with sufficient frequency [1,5]. However, life faced several fundamental challenges in obtaining biologically accessible Fe–S clusters. First, the $(FeS)_1^0$ monomer—a precursor to larger clusters—forms by $Fe(HS)^+$ deprotonation, which is unfavorable at ambient environmental conditions (Table 2). Second, stable [4Fe–4S] cubanes require partial oxidation [34], yet the distribution and concentration of Fe(III) in the Archean ocean is unclear. Third, the strong thermodynamic drive towards $(FeS)_n$(aq) nanosheet polymerization funnels sulfide into mackinawite precipitates, sequestering it in biologically inaccessible mineral phases.

The energetics presented here support picomolar concentrations of oxidized $[2Fe–2S]^+$ rhombs and $[4Fe–4S]^{+/2+}$ cubanes in mildly acidic anoxic seawater, limited primarily by the thermodynamic tendency towards large $(FeS)_n$(aq) nanosheets and their various stacked and water-intercalated analogues. One potential solution to this environmental constraint lies in the presence of chelating bioligands that could mimic or even enhance the stabilizing role of bisulfide coordination shown in Fig. 8B, but at the lower total sulfide conditions characteristic of ferruginous Archean seawater. Coordinating ligands are critical at the bifurcation between nanosheet polymerization and molecular cluster stabilization: bisulfide stabilizes the three-dimensional cubane geometry over two-dimensional sheets, and stronger chelating bioligands would be expected to enhance this effect. The mackinawite-suppressed speciation in Figs. 7B and 8B reveals which aqueous Fe–S species are thermodynamically most favorable in solution, which is information that is obscured when mineral precipitation dominates the total sulfide budget. In synthetic in vitro chemistry, the formation of nanoparticles is prevented by “hiding” the iron ions in a sulfur rich coordination environment (Fe(III) + β-mercaptoethanol) that resembles the rubredoxin metalloprotein's redox active site. First, the β-mercaptoethanol acts as a mild reducing agent to form the ferrous iron. Second, when the tetrathiolate coordinated iron interacts with the bisulfide, the iron remains coordinatively saturated and prevents the formation of the $(FeS)_n$(aq) species. Although cluster concentrations in Archean seawater would have ultimately been limited by mackinawite saturation [1], bioligands that bind cubanes strongly could shift equilibria towards cluster-ligand complexes. By drawing Fe–S from the mineral-buffered pool, such ligands could make clusters bio-obtainable despite low equilibrium concentrations. Cysteine-rich peptides provide a coordination environment that rescues rhombs and cubanes from the nanosheet formation pathways, allowing cluster accumulation without driving the system towards mackinawite supersaturation.

Several thermodynamic and experimental lines of evidence support

the viability of peptide-mediated cluster stabilization. Ligand exchange from bisulfide or water to polydentate peptide sites is energetically strongly favorable due to the entropic advantage of chelation or multidentate binding. Polypeptides with appropriate spacing and amino acids between cysteines adopt conformations (binding pocket or cluster nest) that favorably coordinate clusters [104,105]. In modern metalloenzymes, Fe–S clusters are coordinated by strictly conserved polydentate chelating motifs (Cx_nCy_mC, where x and y are intervening amino acids) [27,31] thought to be ancient molecular fossils [14,17]. Models for such coordinating tri- or tetracysteine peptides [52,53,96,106], which are anionic ligands that combine ionic and covalent interactions, would be expected to significantly inhibit mackinawite-like nanosheet formation and enable localized self-assembly of [2Fe–2S] and [4Fe–4S] molecular clusters.

Such ligands could enhance biologically relevant concentrations of the clusters via Le Chatelier's Principle, shifting all equilibria towards cluster-ligand complexes and promoting assembly and proton oxidation from dissolved Fe and S. Thiolate ligands bind more tightly to the oxidized forms of [4Fe–4S] clusters [107], pulling the bulk speciation towards higher oxidized cubane concentrations. Competition experiments by Petros et al. [52] showed that a model tetrathiolate polypeptide called IGA binds pre-formed $[4Fe–4S]^{2+}$ clusters with a nanomolar dissociation constant, far more strongly than free Fe(II)—though such peptides must still compete for clusters with millimolar free Fe^{2+} concentrations and require deprotonation at mildly acidic Archean seawater pH. Additionally, such ligands can scavenge iron from mineral phases, creating ligand-Fe(II) complexes in mineral-supersaturated environments [1,7].

Our calculations necessarily simplify Archean seawater chemistry but establish a foundation for more complex investigations of Fe–S cluster bio-obtainability. First, although direct experimental validation of Fe(II) coordination geometries at variable pH remains challenging due to speciation changes, precipitate formation, and spectroscopic limitations [101,108], our calculations generate observable predictions for ultraviolet-visible, Raman, X-ray absorption, and Mössbauer spectroscopy studies under carefully controlled anoxic conditions, potentially using microfluidics sample preparation technology. Second, organic thiolates such as β-mercaptoethanol and cysteine are better electron donors than bisulfide and are commonly used in experimental cluster synthesis [25,27,36,97]. Our ongoing DFT modeling of their coordination and redox chemistry will provide information on their bio-obtainability in natural systems that are more directly comparable to laboratory experiments. Models and experiments under ferrous iron-rich conditions with chelating di-thiolates and short peptide maquettes represent further promising steps towards proto-metalloenzyme development. Third, other inorganic components in Archean seawater, such as bicarbonate and polysulfides, may provide additional pathways to stabilize cluster formation [16,25,35,36,109].

Our results suggest that primitive chelating bioligands—perhaps as simple as short cysteine-containing peptides—could have trapped and concentrated Fe–S cluster cofactors directly from Archean Fe(II)-rich, sulfide-bearing seawater. Cluster formation would not have required local enrichments of Fe(III) or oxidants, making these cofactors broadly bio-obtainable throughout Archean oceans. Once primitive life obtained molecular cubane clusters for use in metalloenzymes, strong evolutionary pressure would have driven organisms to explore their chemical reactivity, regulate their binding environment, and control their redox potential, leading to the broad modern diversity of ferredoxins.

5. Conclusions

With combined DFT and aqueous speciation modeling, we show that oxidation of Fe–S complexes and clusters by protons (hydronium to dihydrogen redox or inner-sphere dehydrogenation) is thermodynamically feasible. With this in mind, we propose a scheme where coordinating ligands stabilize both key intermediates and oxidized $[4Fe–4S]^{2+}$ cubanes assembled solely from ferrous iron and sulfide under reducing conditions. Water and, especially, bisulfide are adequate coordinating ligands to stabilize these clusters and outcompete sheet-like cluster precursors to mackinawite precipitates. Furthermore, we found that bisulfide in high enough concentration can drive the dehydrogenation reaction of binuclear clusters. Bisulfide stabilizes molecular clusters, coordinatively saturates iron (which prevents polymerization of nanosheets), and incorporates an oxidative proton in the iron's inner coordination sphere. This, and the established experimental synthesis of clusters stabilized by organic thiolates, suggests that simple chelating bioligands, especially polydentate thiolates, may further support the earliest utilization of cubane clusters.

Even if Fe–S metalloproteins originated in a particular propitious environment, they clearly diversified and evolved throughout Earth history in the oceans, which were Fe(II)-rich for half of Earth history. These results increase the breadth of early Earth environments where cubane clusters may have occurred at micromolar concentrations, permitting evolution to harness their chemical capabilities.

Abbreviations

DFT	density functional theory calculations
SMD	Solvation Model based on Density is an implicit solvation model for reaction field calculations
meta-GGA	meta-generalized gradient approximation
OmPW1PBE	revised version of meta-GGA hybrid functional with Perdew-Wang exchange and Perdew-Burke-Ernzerhof correlation functionals
PBE0	Perdew-Burke-Ernzerhof one-parameter hybrid GGA functional
APF	Austin-Frisch-Petersson mixed hybrid functional from two different GGA functionals
PBE3PBE	Perdew-Burke-Ernzerhof three-parameter hybrid GGA functional
TPSS+D	Exchange and correlation functions from Tao, Perdew, Staroverov, and Scuseria with dispersion correction
X3LYP	mixed hybrid functional by Xu and Goddard from two different GGA functionals
B3PW91+D	Becke's three-parameter hybrid with Perdew-Wang 91 correlation functionals supplemented by dispersion correction
HISSbPBE	Henderson, Izmaylov, Scieseria, and Savin's middle-range hybrid functional with Perdew-Burke-Ernzerhof correlation functional
revTPSS	revised Tao, Perdew, Staroverov, and Scuseria functionals
mPW1LYP	meta-GGA hybrid functional with Perdew-Wang exchange and Lee-Yang-Parr correlation functionals
OmPW1LYP	revised version of mPW1LYP functional.
B3P86	Becke's three-parameter hybrid with Perdew 86 correlation functional
wB97XD	range-separated Becke 97 exchange and correlation functionals with dispersion correction
TPSSh	Hybrid meta-GGA functional developed from the TPSS functionals
OmPW3PBE	revised version of three-parametric hybrid Perdew-Wang exchange and Lee-Yang-Parr correlation functional
tHCTHhyb	Hybrid functional using the kinetic-energy density (t) HCTH-functional
HCTH147	Hamprecht, Cohen, Tozer, and Handy least-square fitted functional for 147 molecular systems with 15 parameters
PHREEQC	USGS-developed software for modeling aqueous geochemistry
Minteq	USEPA-developed speciation database

CRediT authorship contribution statement

Theodore M. Present: Writing – review & editing, Writing – original draft, Visualization, Validation, Software, Methodology, Investigation, Formal analysis, Data curation, Conceptualization. **Joan Selverstone Valentine:** Writing – review & editing, Supervision, Project administration, Methodology, Conceptualization. **Jena E. Johnson:** Writing – review & editing, Supervision, Conceptualization. **Robert K. Szilagyi:** Writing – review & editing, Writing – original draft, Visualization, Validation, Supervision, Software, Resources, Project administration, Methodology, Investigation, Funding acquisition, Formal analysis, Data curation, Conceptualization.

Declaration of competing interest

The authors declare that they have no known competing financial interests or personal relationships that could have appeared to influence the work reported in this paper.

Acknowledgements

TMP was supported by Simons Foundation Grant 668346. Financial support from the UBC Aspire program to RKSz is gratefully acknowledged. Thermochemical calculations were made possible by the Advanced Research Computing at the University of British Columbia (arc.ubc.ca), and the Digital Research Alliance of Canada (alliancecan.ca). We thank Prof. John Dawson for editorial handling and the privilege of contributing to this special issue in honor of Harry Gray, and two anonymous reviewers for insightful and constructive efforts.

Appendix A. OMPW1PBE functional calculated chemical equilibria

Continuum only, no explicit water solvation	ΔG° (ΔH°) in kJ/mol
Precursor assembly	
$Fe(II)(aq) + HS^-(aq) \Leftrightarrow Fe(SH)^+(aq)$	−8 (−11)
$Fe(SH)^+ + H_2O \Leftrightarrow FeS + H_3O^+$	+100 (+72)
$Fe(SH)^+ + HO^- \Leftrightarrow FeS + H_2O$	−132 (−160)
Clustering of reduced species	
2 [FeS] ⇔ [2Fe—2S]	−121 (−174)
2 [2Fe—2S] ⇔ [4Fe—4S]	+37 (−15)
$3\ FeS \Leftrightarrow (FeS)_3$	−198 (−297)
$[2Fe—2S] + FeS \Leftrightarrow (FeS)_3$	−77 (−123)
$4\ FeS \Leftrightarrow (FeS)_4$, bent at Fe site	−428 (−276)
$4\ FeS \Leftrightarrow (FeS)_4$, bent at S site	−399 (−252)
$4\ FeS \Leftrightarrow (FeS)_4$, linear/zigzag	−274 (−427)
4 FeS ⇔ [4Fe—4S]	−205 (−363)
zigzag $(FeS)_4$ ⇔ cubane [4Fe—4S]	+69 (+64)
Oxidation by proton	
$FeS + H_3O^+ \Leftrightarrow [FeS]^+ + H_2O + ½\ H_2$	−70 (−55)
$Fe(SH)^+ + H_3O^+ \Leftrightarrow Fe(SH)^{2+} + H_2O + ½\ H_2$	+94 (+110)
$FeCl^+ + H_3O^+ \Leftrightarrow FeCl^{2+} + H_2O + ½\ H_2$	+146 (+161)
$[2Fe—2S] + H_3O^+ \Leftrightarrow [2Fe—2S]^+ + H_2O + ½\ H_2$	−60 (−40)
Clustering of oxidized species	
$[2Fe\text{-}2S] + [2Fe—2S]^+ \Leftrightarrow [4Fe—4S]^+$	−14 (−163)
$2\ [2Fe—2S]^+ \Leftrightarrow [4Fe—4S]^{2+}$	−52 (−112)

Continuum and Explicit Water solvation:	ΔG° (ΔH°) in kJ/mol
Precursor assembly.	
$Fe(II)x6W + HS^-x4W \Leftrightarrow Fe(SH)^+x5W + H_2Ox4W$	−20 (−23)
$Fe(SH)^+\times 5\ W + HS^-\times 4W \Leftrightarrow Fe(SH)_2\times 5\ W + 4W$	+10 (−6)
$Fe(II)\times 6\ W + HS^-\times 4W \Leftrightarrow (FeS)_1\times 5\ W + H_3O^+\times 4W$	+83 (+88)
$Fe(II)\times 6\ W + H_2S\times 4W + H_2O\times 4W \Leftrightarrow (FeS)_1^+\times 5\ W + 2H_3O^+\times 4W$	+105 (+97)
$Fe(SH)^+\times 5\ W + H_2O\times 4W \Leftrightarrow (FeS)_1\times 5\ W + H_3O^+\times 4W$	+103 (+111)
$Fe(SH)^+\times 5\ W + HO^-\times 4W \Leftrightarrow (FeS)_1\times 5\ W + H_2O\times 4W$	+10 (+14)
Clustering of reduced species	
$2\ (FeS)_1\times 5\ W \Leftrightarrow [2Fe—2S]$ or $(FeS)_2 + 2\ H_2O\times 4W$	−88 (−38)
$2\ (FeS)_1\times 5\ W \Leftrightarrow [2Fe—2S]$ or $(FeS)_2 + 2\ 5\ W$	−93 (−65)
$2\ [2Fe—2S]\times 2\ W \Leftrightarrow [4Fe—4S]\times 4W$	−52 (−98)
$(FeS)_2 + (FeS)_1\times 5\ W \Leftrightarrow (FeS)_3 + 5\ W$	−63 (−68)
$(FeS)_3 + (FeS)_1\times 5\ W \Leftrightarrow (FeS)_4 + 5\ W$	
$(FeS)_3 + (FeS)_1\times 5\ W \Leftrightarrow (FeS)_4 + 5\ W$, bent at Fe site	−65 (−76)
$(FeS)_3 + (FeS)_1\times 5\ W \Leftrightarrow (FeS)_4 + 5\ W$, bent at S site	−41 (−48)
$(FeS)_3 + (FeS)_1\times 5\ W \Leftrightarrow (FeS)_4 + 5\ W$, zigzag	−62 (−76)
Oxidation by proton	
$(FeS)_1\times 5\ W + H_3O^+\times 4W \Leftrightarrow (FeS)_1^+\times 5\ W + H_2O\times 4W + ½\ H_2$	+0.4 (+11)
$Fe(SH)^+\times 5\ W + H_3O^+\times 4W \Leftrightarrow Fe(SH)^{2+}\times 5\ W + H_2O\times 5\ W + ½\ H_2$	+90(+111)
$[2Fe—2S] + H_3O^+\times 4W \Leftrightarrow [2Fe—2S]^+ + H_2O\times 4W + ½\ H_2$	+8 (+33)
$[2Fe—2S]\times 2\ W + H_3O^+\times 4W \Leftrightarrow [2Fe—2S]^+\times 2\ W + H_2O\times 4W + ½\ H_2$	−8 (+19)
$[4Fe—4S]\times 4W + H_3O^+\times 4W \Leftrightarrow [4Fe—4S]^+\times 4W + ½\ H_2 + H_2O\times 4W$	−17 (−46)
$[4Fe—4S]^+\times 4W + H_3O^+\times 4W \Leftrightarrow [4Fe—4S]^{2+}\times 4W + ½\ H_2 + H_2O\times 4W$	+45(+51)

(continued on next page)

(*continued*)

Continuum and Explicit Water solvation:	ΔG° (ΔH°) in kJ/mol
$[2Fe\text{-}2S(SH)_2]^{2-} + H_3O^+ \times 4W \Leftrightarrow [2Fe\text{-}2S(SH)_2]^- + ½\ H_2 + H_2O \times 4W$	−26 (−4)
Clustering of oxidized species	
$(FeS)_1 \times 5\ W + (FeS)_1^+ \times 5\ W \Leftrightarrow [2Fe—2S]^+ \times 2\ W + 2\ 4W$	−124 (−83)
$2\ (FeS)_1^+ \times 5\ W \Leftrightarrow [2Fe—2S]^{2+} \times 2\ W + 2\ 4W$	−31 (−11)
$(FeS)_1 \times 5\ W + (FeS)_1^+ \times 5\ W \Leftrightarrow [2Fe—2S]^+ \times 4W + 6\ W$	−100 (−102)
$[2Fe—2S] \times 2\ W + [2Fe—2S]^+ \times 2\ W \Leftrightarrow [4Fe—4S]^+ \times 4W$	−78 (−160)
$2\ [2Fe—2S]^+ \times 2\ W \Leftrightarrow [4Fe—4S]^{2+} \times 4W$	−42 (−121)
Dimerization of the $Fe(SH)^+$	
$2\ Fe(SH)^+ \times 5\ W \Leftrightarrow [2Fe\text{-}2(SH)]^{2+} + 2\ H_2O \times 4W$	+51 (+133)
$2\ Fe(SH)^+ \times 5\ W \Leftrightarrow [2Fe\text{-}2(SH)]^{2+} \times 2\ W + 2\ 4W$	+6 (+61)
$2\ Fe(SH)^+ \times 5\ W \Leftrightarrow [2Fe\text{-}2(SH)]^{2+} \times 4W + 6\ W.$	+5 (+23)
Deprotonation of the $Fe(SH)^+$ dimer	
$[2Fe\text{-}2(SH)]^{2+} \times 2\ W + 2\ H_2O \times 4W \Leftrightarrow [2Fe—2S] \times 2\ W + 2\ H_3O^+ \times 4W$	+84 (+70)
$[2Fe\text{-}2(SH)]^{2+} \times 4W + 2\ H_2O \times 4W \Leftrightarrow [2Fe—2S] \times 4W + 2\ H_3O^+ \times 4W$	+122 (+121)
$[2Fe\text{-}2(SH)]^{2+} \times 2\ W + 2\ HO^- \times 4W \Leftrightarrow [2Fe—2S] \times 2\ W + 2\ H_2O \times 4W$	−102 (−125)
$[2Fe\text{-}2(SH)]^{2+} \times 4W + 2\ HO^- \times 4W \Leftrightarrow [2Fe—2S] \times 4W + 2\ H_2O \times 4W$	−64 (−74)
Dehydrogenation of the $Fe(SH)^+$ dimer	
$[2Fe\text{-}2(SH)]^{2+} \times 2\ W \Leftrightarrow [2Fe—2S]^{2+} \times 2\ W + H_2$	+169 (+195)
$[2Fe\text{-}2(SH)]^{2+} \times 4W + 4W \Leftrightarrow [2Fe—2S]^{2+} \times 2\ W + H_2 + 6\ W$	+127 (+135)
$[2Fe\text{-}2(SH)(SH)_2] \Leftrightarrow [2Fe\text{-}2S(SH)_2]^{2+} + H_2$	+98 (+122)
$[2Fe\text{-}2(SH)(SH)_2] + 2\ HS^- \times 4W \Leftrightarrow [2Fe\text{-}2S(SH)_4]^{2-} + H_2 \times 2\ W + 6\ W$	−5 (−3)
$[2Fe\text{-}2(SH)(SH)_2] + 2\ HS^- \times 4W \Leftrightarrow [2Fe\text{-}2S(SH)_4]^{2-} + H_2 + 2\ 4W$	−27 (−20)
$[2Fe\text{-}2S(SH)_4]^{2-} + [2Fe—2S] \Leftrightarrow [4Fe\text{-}4S(HS)_4]^{2-}$	−117 (−175)
HS^- saturating Fe-sites and ligand exchange	
$[2Fe—2S] + 2\ HS^- \times 4W \Leftrightarrow [2Fe\text{-}2S(SH)_2]^{2-} + 2\ 4W$	−50 (−72)
$2\ [2Fe\text{-}2S(SH)_2]^{2-} \Leftrightarrow [4Fe\text{-}4S(SH)_4]^{4-}$	+6 (−55)
$[2Fe\text{-}2S(SH)_2]^{2-} + [2Fe\text{-}2S(SH)_2]^- \Leftrightarrow [4Fe\text{-}4S(SH)_4]^{3-}$	−94 (−157)
$2\ [2Fe\text{-}2S(SH)_2]^- \Leftrightarrow [4Fe\text{-}4S(SH)_4]^{2-}$	−123 (−189)
$2\ [2Fe—2S]x2W + 4\ HS^- x4W \Leftrightarrow [4Fe\text{-}4S(HS)_4]^{4-} + 4\ 5\ W$	−48 (−145)
$[2Fe—2S]x2W + [2Fe—2S]^+ x2W + 4\ HS^- x4W \Leftrightarrow [4Fe\text{-}4S(HS)_4]^{3-} + 4\ 5\ W$	−166 (−271)
$2\ [2Fe—2S]^+ x2W + 4\ HS^- x4W \Leftrightarrow [4Fe\text{-}4S(HS)_4]^{2-} + 4\ 5\ W$	-212 (−326)
$[4Fe—4S] \times 4W + 4\ HS^- x4W \Leftrightarrow [4Fe\text{-}4S(HS)_4]^{4-} + 4\ 5\ W$	+4 (−46)
$[4Fe—4S]^+ \times 4W + 4\ HS^- x4W \Leftrightarrow [4Fe\text{-}4S(HS)_4]^{3-} + 4\ 5\ W$	−88 (−110)
$[4Fe—4S]^{2+} \times 4W + 4\ HS^- x4W \Leftrightarrow [4Fe\text{-}4S(HS)_4]^{2-} + 4\ 5\ W$	−170 (−206)
H_2S oxidation	
$[2Fe\text{-}2S] + 2\ H_2S \times 4W + 4W \Leftrightarrow [2Fe—2S]^{2+} \times 4W + 2\ HS^- \times 4W + H_2$	+93 (+46).
$[2Fe—2S] + 2\ H_2S \times 4W \Leftrightarrow [2Fe\text{-}2S(SH)_2] + H_2 + 2\ 4W$	+13 (−6)
$[2Fe—2S] + 2\ H_2S \times 4W + 2\ HS^- \times 4W \Leftrightarrow [2Fe\text{-}2S(SH)_4]^{2-} + H_2 + 4\ 4W$	−112 (−148)
Water entering inner sphere	
$FeS(aq) + 5\ W \Leftrightarrow (FeS)_1 \times 5\ W$	−16 (−68)
$[2Fe—2S] + 6\ W \Leftrightarrow [2Fe—2S] \times 2\ W + 4W$	−19 (−30)
$[2Fe—2S]^+ + 6\ W \Leftrightarrow [2Fe—2S]^+ \times 2\ W + 4W$	−34 (−44)
$[2Fe—2S]^{2+} + 6\ W \Leftrightarrow [2Fe—2S]^{2+} \times 2\ W + 4W$	−42 (−59)
$[2Fe—2S]^{2+} + 2\ 6\ W \Leftrightarrow [2Fe—2S]^{2+} \times 4W + 2\ 4W$	−89 (−123)
$[2Fe—2S] \times 2\ W + 6\ W \Leftrightarrow [2Fe—2S] \times 4W + 4W$	+13 (+19)
$[4Fe—4S] + 4W \Leftrightarrow [4Fe—4S] \times 4W$	−102 (−151)
$[4Fe—4S]^+ + 4W \Leftrightarrow [4Fe—4S]^+ \times 4W$	−7 (−78)
$[4Fe—4S]^{2+} + 4W \Leftrightarrow [4Fe—4S]^{2+} \times 4W$	−37 (−108)
$(FeS)_4 + 4W \Leftrightarrow (FeS)_4 \times 4W$	
$(FeS)_4 + 4W \Leftrightarrow (FeS)_4 \times 4W$, zigzag	+30 (−21)
$(FeS)_4 + 4W \Leftrightarrow (FeS)_4 \times 4W$, bent at Fe	+11 (−40)
$(FeS)_4 + 4W \Leftrightarrow (FeS)_4 \times 4W$, bent at S	+32 (−13)
$[2Fe\text{-}2(SH)]^{2+} + 6\ W \Leftrightarrow [2Fe\text{-}2(SH)]^{2+} \times 2\ W + 4W$	−36 (−49)
$[2Fe\text{-}2(SH)]^{2+} + 4W \Leftrightarrow [2Fe\text{-}2(SH)]^{2+} \times 4W$	−37 (−87)

Appendix B. Supplementary data

Supplementary data to this article can be found online at https://doi.org/10.1016/j.jinorgbio.2026.113259. Additional Supporting Information with atomic positional coordinates, electronic structures in formatted checkpoint files, scripts, analysis tools, PHREEQC database files, and PhreePlot plotting files are also made available at DOI: 10.5281/zenodo.18548202.

References

[1] J.E. Johnson, T.M. Present, J.S. Valentine, Iron: life's primeval transition metal, Proc. Natl. Acad. Sci. 121 (2024) e2318692121, https://doi.org/10.1073/pnas.2318692121.

[2] E.-I. Ochiai, The evolution of the environment and its influence on the evolution of life, Orig. Life 9 (1978) 81–91, https://doi.org/10.1007/BF00931406.

[3] R.E.M. Rickaby, Goldilocks and the three inorganic equilibria: how earth's chemistry and life coevolve to be nearly in tune, Philos. Trans. R. Soc. A Math. Phys. Eng. Sci. 373 (2015) 20140188, https://doi.org/10.1098/rsta.2014.0188.

[4] R.J.P. Williams, The natural selection of the chemical elements, Cell. Mol. Life Sci. 53 (1997) 816–829, https://doi.org/10.1007/s000180050102.

[5] R.J.P. Williams, R.E.M. Rickaby, Evolution's Destiny: co-evolving chemistry of the environment and life, Royal Society of Chemistry, Cambridge, 2012, https://doi.org/10.1039/9781849735599.

[6] J.J.R. Frausto da Silva, R.J.P. Williams, The Biological Chemistry of the Elements: The Inorganic Chemistry of Life, OUP Oxford, 2001.

[7] M.A. Saito, D.M. Sigman, F.M.M. Morel, The bioinorganic chemistry of the ancient ocean: the co-evolution of cyanobacterial metal requirements and biogeochemical cycles at the Archean–Proterozoic boundary? Inorg. Chim. Acta 356 (2003) 308–318, https://doi.org/10.1016/S0020-1693(03)00442-0.

[8] C. Andreini, I. Bertini, G. Cavallaro, G.L. Holliday, J.M. Thornton, Metal ions in biological catalysis: from enzyme databases to general principles, JBIC J. Biol. Inorg. Chem. 13 (2008) 1205–1218, https://doi.org/10.1007/s00775-008-0404-5.

[9] C.D. Okafor, J.C. Bowman, N.V. Hud, J.B. Glass, L.D. Williams, Folding and catalysis near life's origin: Support for Fe2+ as a dominant divalent cation, in: C. Menor-Salván (Ed.), Prebiotic Chem. Chem. Evol. Nucleic Acids, Springer International Publishing, Cham, 2018, pp. 227–243, https://doi.org/10.1007/978-3-319-93584-3_8.

[10] H.B. Gray, B.G. Malmstroem, Long-range electron transfer in multisite metalloproteins, Biochemistry 28 (1989) 7499–7505, https://doi.org/10.1021/bi00445a001.

[11] D.C. Johnson, D.R. Dean, A.D. Smith, M.K. Johnson, Structure, function, and formation of biological Iron-sulfur clusters, Annu. Rev. Biochem. 74 (2005) 247–281, https://doi.org/10.1146/annurev.biochem.74.082803.133518.

[12] H. Beinert, Iron-sulfur proteins: ancient structures, still full of surprises, JBIC J. Biol. Inorg. Chem. 5 (2000) 2–15, https://doi.org/10.1007/s007750050002.

[13] J.D. Pritts, S.L.J. Michel, Fe-S clusters masquerading as zinc finger proteins, J. Inorg. Biochem. 230 (2022) 111756, https://doi.org/10.1016/j.jinorgbio.2022.111756.

[14] D.O. Hall, R. Cammack, K.K. Rao, The iron-Sulphur proteins: evolution of a ubiquitous protein from model systems to higher organisms, Orig. Life 5 (1974) 363–386, https://doi.org/10.1007/BF01207637.

[15] M.J. Russell, R.M. Daniel, A.J. Hall, J.A. Sherringham, A hydrothermally precipitated catalytic iron sulphide membrane as a first step toward life, J. Mol. Evol. 39 (1994) 231–243, https://doi.org/10.1007/BF00160147.

[16] M.J. Russell, A. Hall, The emergence of life from iron monosulphide bubbles at a submarine hydrothermal redox and pH front, J. Geol. Soc. Lond. 154 (1997) 377–402.

[17] R.V. Eck, M.O. Dayhoff, Evolution of the structure of ferredoxin based on living relics of primitive amino acid sequences, Science 152 (1966) 363–366, https://doi.org/10.1126/science.152.3720.363.

[18] D.O. Hall, R. Cammack, K.K. Rao, Role for ferredoxins in the origin of life and biological evolution, Nature 233 (1971) 136–138, https://doi.org/10.1038/233136a0.

[19] D.C. Rees, Great metalloclusters in enzymology, Annu. Rev. Biochem. 71 (2002) 221–246, https://doi.org/10.1146/annurev.biochem.71.110601.135406.

[20] G. Wächtershäuser, Before enzymes and templates: theory of surface metabolism, Microbiol. Rev. 52 (1988) 452–484, https://doi.org/10.1128/mr.52.4.452-484.1988.

[21] S.A. Sanden, R.K. Szilagyi, Y. Li, N. Kitadai, S.M. Webb, T. Yano, R. Nakamura, M. Hara, S.E. McGlynn, Electrochemically induced metal- *vs.* ligand-based redox changes in mackinawite: identification of a Fe^{3+} – and polysulfide-containing intermediate, Dalton Trans. 50 (2021) 11763–11774, https://doi.org/10.1039/D1DT01684A.

[22] D. Rickard, G.W. Luther, Chemistry of Iron sulfides, Chem. Rev. 107 (2007) 514–562, https://doi.org/10.1021/cr0503658.

[23] T. Douglas, D.P.E. Dickson, S. Betteridge, J. Charnock, C.D. Garner, S. Mann, Synthesis and structure of an Iron(III) sulfide-ferritin bioinorganic nanocomposite, Science 269 (1995) 54–57, https://doi.org/10.1126/science.269.5220.54.

[24] G.W. Luther, D.T. Rickard, Metal sulfide cluster complexes and their biogeochemical importance in the environment, J. Nanopart. Res. 7 (2005) 389–407, https://doi.org/10.1007/s11051-005-4272-4.

[25] S.F. Jordan, I. Ioannou, H. Rammu, A. Halpern, L.K. Bogart, M. Ahn, R. Vasiliadou, J. Christodoulou, A. Maréchal, N. Lane, Spontaneous assembly of redox-active iron-sulfur clusters at low concentrations of cysteine, Nat. Commun. 12 (2021) 5925, https://doi.org/10.1038/s41467-021-26158-2.

[26] L. Grunwald, M. Clémancey, D. Klose, L. Dubois, S. Gambarelli, G. Jeschke, M. Wörle, G. Blondin, V. Mougel, A complete biomimetic iron-sulfur cubane redox series, Proc. Natl. Acad. Sci. 119 (2022) e2122677119, https://doi.org/10.1073/pnas.2122677119.

[27] P.V. Rao, R.H. Holm, Synthetic analogues of the active sites of Iron−sulfur proteins, Chem. Rev. 104 (2004) 527–560, https://doi.org/10.1021/cr020615+.

[28] F. Capozzi, S. Ciurli, C. Luchinat, Coordination sphere versus protein environment as determinants of electronic and functional properties of iron-sulfur proteins, in: H.A.O. Hill, P.J. Sadler, A.J. Thomson (Eds.), Met. Sites Proteins Models Redox Cent., Springer, Berlin, Heidelberg, 1998, pp. 127–160, https://doi.org/10.1007/3-540-62888-6_5.

[29] W. Yao, P.M. Gurubasavaraj, P.L. Holland, All-Ferrous Iron–Sulfur Clusters, in: D. Rabinovich (Ed.), Mol. Des. Inorg. Biochem., Springer Berlin Heidelberg, Berlin, Heidelberg, 2012, pp. 1–37, https://doi.org/10.1007/430_2012_81.

[30] W. Sweeney, J. Rabinowitz, D. Yoch, High and low reduction potential 4Fe-4S clusters in Azotobacter vinelandii (4Fe-4S) 2ferredoxin I. Influence of the polypeptide on the reduction potentials, J. Biol. Chem. 250 (1975) 7842–7847, https://doi.org/10.1016/S0021-9258(19)40892-2.

[31] C. Bonfio, The curious case of peptide-coordinated iron–sulfur clusters: prebiotic and biomimetic insights, Dalton Trans. 50 (2021) 801–807, https://doi.org/10.1039/D0DT03947K.

[32] R. Szilagyi, Multi-edge X-ray Absorption Spectroscopic Evidence for Sulphur-based Redox in [4Fe-4S] Molecular Clusters, 2024, https://doi.org/10.26434/chemrxiv-2024-q3v7b.

[33] H.C. Angove, S.J. Yoo, B.K. Burgess, E. Münck, Mössbauer and EPR evidence for an all-ferrous Fe4S4 cluster with S = 4 in the Fe protein of Nitrogenase, J. Am. Chem. Soc. 119 (1997) 8730–8731, https://doi.org/10.1021/ja9712837.

[34] C. Bonfio, L. Valer, S. Scintilla, S. Shah, D.J. Evans, L. Jin, J.W. Szostak, D. D. Sasselov, J.D. Sutherland, S.S. Mansy, UV-light-driven prebiotic synthesis of iron–sulfur clusters, Nat. Chem. 9 (2017) 1229–1234, https://doi.org/10.1038/nchem.2817.

[35] L. Valer, Y.J. Hu, A. Cini, M. Lantieri, C.R. Walton, O. Shorttle, M. Fittipaldi, S. S. Mansy, Prebiotic environmental conditions impact the type of Iron-sulfur cluster formed, ChemSystemsChem 7 (2025) e202400051, https://doi.org/10.1002/syst.202400051.

[36] J. Li, S.A. Pearson, K.D. Fenk, J.A. Cowan, Glutathione-coordinated [2Fe–2S] cluster is stabilized by intramolecular salt bridges, JBIC J. Biol. Inorg. Chem. 20 (2015) 1221–1227, https://doi.org/10.1007/s00775-015-1301-3.

[37] G. Christou, C.D. Garner, A convenient synthesis of tetrakis[thiolato-μ_3-sulphido-iron](2–) clusters, J. Chem. Soc. Dalton Trans. (1979) 1093–1094, https://doi.org/10.1039/DT9790001093.

[38] K.S. Hagen, J.G. Reynolds, R.H. Holm, Definition of reaction sequences resulting in self-assembly of [Fe4S4(SR)4]2- clusters from simple reactants, J. Am. Chem. Soc. 103 (1981) 4054–4063, https://doi.org/10.1021/ja00404a013.

[39] F. Bonomi, M.T. Werth, D.M. Kurtz, Assembly of [FenSn(SR)4]2- (n = 2, 4) in aqueous media from iron salts, thiols, and sulfur, sulfide, or thiosulfate plus rhodanese, Inorg. Chem. 24 (1985) 4331–4335, https://doi.org/10.1021/ic00219a026.

[40] M. Invernici, G. Selvolini, J.M. Silva, G. Marrazza, S. Ciofi-Baffoni, M. Piccioli, Interconversion between [2Fe–2S] and [4Fe–4S] cluster glutathione complexes, Chem. Commun. 58 (2022) 3533–3536, https://doi.org/10.1039/D1CC03566E.

[41] E.S. Boyd, K.M. Thomas, Y. Dai, J.M. Boyd, F.W. Outten, Interplay between oxygen and Fe–S cluster biogenesis: insights from the Suf pathway, Biochemistry 53 (2014) 5834–5847, https://doi.org/10.1021/bi500488r.

[42] F.A. Armstrong, R.J.P. Williams, Thermodynamic infuences on the identity of iron-Sulphur cluster formation in proteins, FEBS Lett. 451 (1999) 91–94.

[43] D.I. Arnon, Ferredoxin and photosynthesis: an iron-containing protein is a key factor in energy transfer during photosynthesis, Science 149 (1965) 1460–1470, https://doi.org/10.1126/science.149.3691.1460.

[44] K. Tagawa, D.I. Arnon, Ferredoxins as electron carriers in photosynthesis and in the biological production and consumption of hydrogen gas, Nature 195 (1962) 537–543, https://doi.org/10.1038/195537a0.

[45] C. Drennan, Surprising cofactors in metalloenzymes, Curr. Opin. Struct. Biol. 13 (2003) 220–226, https://doi.org/10.1016/S0959-440X(03)00038-1.

[46] D. Rickard, G.W. Luther, Kinetics of pyrite formation by the H2S oxidation of iron (II) monosulfide in aqueous solutions between 25 and 125°C: the mechanism, Geochim. Cosmochim. Acta 61 (1997) 135–147, https://doi.org/10.1016/S0016-7037(96)00322-5.

[47] A. Lennie, D.J. Vaughan, Spectroscopic Studies of iron Sulfide Formation and Phase Relations at Low Temperatures, in: Miner. Spectrosc. Tribute Roger G Bums, The Geochemical Society, 1996.

[48] N.J. Tosca, I.A.M. Ahmed, B.M. Tutolo, A. Ashpitel, J.A. Hurowitz, Magnetite authigenesis and the warming of early Mars, Nat. Geosci. 11 (2018) 635–639, https://doi.org/10.1038/s41561-018-0203-8.
[49] M. Preiner, J.C. Xavier, F.L. Sousa, V. Zimorski, A. Neubeck, S.Q. Lang, H. C. Greenwell, K. Kleinermanns, H. Tüysüz, T.M. McCollom, N.G. Holm, W. F. Martin, Serpentinization: connecting geochemistry, ancient metabolism and industrial hydrogenation, Life 8 (2018) 41, https://doi.org/10.3390/life8040041.
[50] A.S. Templeton, E.T. Ellison, Formation and loss of metastable brucite: does Fe (II)-bearing brucite support microbial activity in serpentinizing ecosystems? Philos. Trans. R. Soc. A Math. Phys. Eng. Sci. 378 (2020) 20180423, https://doi.org/10.1098/rsta.2018.0423.
[51] L. Valer, D. Rossetto, T. Parkkila, L. Sebastianelli, G. Guella, A.L. Hendricks, J. A. Cowan, L. Sang, S.S. Mansy, Histidine ligated Iron-sulfur peptides, ChemBioChem 23 (2022) e202200202, https://doi.org/10.1002/cbic.202200202.
[52] A.K. Petros, A.R. Reddi, M.L. Kennedy, A.G. Hyslop, B.R. Gibney, Femtomolar Zn (II) affinity in a peptide-based ligand designed to model thiolate-rich Metalloprotein active sites, Inorg. Chem. 45 (2006) 9941–9958, https://doi.org/10.1021/ic052190q.
[53] B.R. Gibney, S.E. Mulholland, F. Rabanal, P.L. Dutton, Ferredoxin and ferredoxin–heme maquettes, Proc. Natl. Acad. Sci. 93 (1996) 15041–15046, https://doi.org/10.1073/pnas.93.26.15041.
[54] S.E. Mulholland, B.R. Gibney, F. Rabanal, P.L. Dutton, Characterization of the fundamental protein ligand requirements of [4Fe-4S]2+/+ clusters with sixteen amino acid Maquettes, J. Am. Chem. Soc. 120 (1998) 10296–10302, https://doi.org/10.1021/ja981279a.
[55] S. Haider, D. Di Tommaso, N.H. De Leeuw, Density functional theory simulations of the structure, stability and dynamics of iron sulphide clusters in water, Phys. Chem. Chem. Phys. 15 (2013) 4310, https://doi.org/10.1039/c3cp43560a.
[56] T.V. Harris, R.K. Szilagyi, Iron–sulfur bond covalency from electronic structure calculations for classical iron–sulfur clusters, J. Comput. Chem. 35 (2014) 540–552, https://doi.org/10.1002/jcc.23518.
[57] R.K. Szilagyi, M.A. Winslow, On the accuracy of density functional theory for iron—sulfur clusters, J. Comput. Chem. 27 (2006) 1385–1397, https://doi.org/10.1002/jcc.20449.
[58] D. Rappoport, F. Furche, Property-optimized Gaussian basis sets for molecular response calculations, J. Chem. Phys. 133 (2010) 134105, https://doi.org/10.1063/1.3484283.
[59] M. Kour, A. Taborosi, E.S. Boyd, R.K. Szilagyi, Development of molecular cluster models to probe pyrite surface reactivity, J. Comput. Chem. 44 (2023) 2486–2500, https://doi.org/10.1002/jcc.27213.
[60] T.V. Harris, R.K. Szilagyi, Comparative assessment of the composition and charge state of Nitrogenase FeMo-cofactor, Inorg. Chem. 50 (2011) 4811–4824, https://doi.org/10.1021/ic102446n.
[61] A.V. Marenich, C.J. Cramer, D.G. Truhlar, Universal solvation model based on solute Electron Density and on a continuum model of the solvent defined by the bulk dielectric constant and atomic surface tensions, J. Phys. Chem. B 113 (2009) 6378–6396, https://doi.org/10.1021/jp810292n.
[62] D.L. Parkhurst, C.A.J. Appelo, Description of Input and Examples for PHREEQC Version 3—A Computer Program for Speciation, Batch-Reaction, One-Dimensional Transport, and Inverse Geochemical Calculations, U.S. Geological Survey, Reston, Virginia, 2013, p. 497. https://pubs.usgs.gov/tm/06/a43/.
[63] D.G. Kinniburgh, D.M. Cooper, PhreePlot. https://www.phreeplot.org, 2011 (accessed June 19, 2020).
[64] J.D. Allison, D.S. Brown, K.J. Novo-Gradac, MINTEQA2/PRODEFA2, a Geochemical Assessment Model for Environmental Systems: Version 3.0 User's Manual, U.S. Environmental Protection Agency, Athens, Georgia, 1991. https://www.epa.gov/sites/default/files/documents/USERMANU.PDF.
[65] HydroGeoLogic, Inc., Allison Geoscience Consultants, Inc., MINTEQA2/PRODEFA2, A Geochemical Assessment Model for Environmental Systems: User Manual Supplement for Version 4.0, U.S. Environmental Protection Agency, Athens, Georgia, 1999. https://www.epa.gov/sites/default/files/documents/SUPPLE1.PDF (accessed May 11, 2022).
[66] D. Rickard, G.W. Luther, Metal sulfide complexes and clusters, Rev. Mineral. Geochem. 61 (2006) 421–504, https://doi.org/10.2138/rmg.2006.61.8.
[67] D. Rickard, The solubility of FeS, Geochim. Cosmochim. Acta 70 (2006) 5779–5789, https://doi.org/10.1016/j.gca.2006.02.029.
[68] I. Halevy, A. Bachan, The geologic history of seawater pH, Science 355 (2017) 1069–1071, https://doi.org/10.1126/science.aal4151.
[69] M. Mammen, E.I. Shakhnovich, J.M. Deutch, G.M. Whitesides, Estimating the entropic cost of self-assembly of multiparticle hydrogen-bonded aggregates based on the cyanuric acid·melamine lattice, J. Organomet. Chem. 63 (1998) 3821–3830, https://doi.org/10.1021/jo970944f.
[70] D. Dyrssen, K. Kremling, Increasing hydrogen sulfide concentration and trace metal behavior in the anoxic Baltic waters, Mar. Chem. 30 (1990) 193–204, https://doi.org/10.1016/0304-4203(90)90070-S.
[71] A. Austin, G.A. Petersson, M.J. Frisch, F.J. Dobek, G. Scalmani, K. Throssell, A density functional with spherical atom dispersion terms, J. Chem. Theory Comput. 8 (2012) 4989–5007, https://doi.org/10.1021/ct300778e.
[72] J.P. Perdew, K. Burke, M. Ernzerhof, Generalized gradient approximation made simple, Phys. Rev. Lett. 77 (1996) 3865–3868, https://doi.org/10.1103/PhysRevLett.77.3865.
[73] C. Lee, W. Yang, R.G. Parr, Development of the Colle-Salvetti correlation-energy formula into a functional of the electron density, Phys. Rev. B 37 (1988) 785–789, https://doi.org/10.1103/PhysRevB.37.785.
[74] A.D. Becke, Density-functional exchange-energy approximation with correct asymptotic behavior, Phys. Rev. A 38 (1988) 3098–3100, https://doi.org/10.1103/PhysRevA.38.3098.
[75] F.A. Hamprecht, A.J. Cohen, D.J. Tozer, N.C. Handy, Development and assessment of new exchange-correlation functionals, J. Chem. Phys. 109 (1998) 6264–6271, https://doi.org/10.1063/1.477267.
[76] J. Tao, J.P. Perdew, V.N. Staroverov, G.E. Scuseria, Climbing the density functional ladder: nonempirical meta–generalized gradient approximation designed for molecules and solids, Phys. Rev. Lett. 91 (2003) 146401, https://doi.org/10.1103/PhysRevLett.91.146401.
[77] A.D. Boese, N.C. Handy, New exchange-correlation density functionals: the role of the kinetic-energy density, J. Chem. Phys. 116 (2002) 9559–9569, https://doi.org/10.1063/1.1476309.
[78] R. Peverati, D.G. Truhlar, M11-L: a local Density functional that provides improved accuracy for electronic structure calculations in chemistry and physics, J. Phys. Chem. Lett. 3 (2012) 117–124, https://doi.org/10.1021/jz201525m.
[79] R.L. Martin, P.J. Hay, L.R. Pratt, Hydrolysis of ferric ion in water and conformational equilibrium, J. Phys. Chem. A 102 (1998) 3565–3573, https://doi.org/10.1021/jp980229p.
[80] A. Riefer, M. Hackert-Oschätzchen, P. Plänitz, G. Meichsner, Characterization of iron(III) in aqueous and alkaline environments with ab initio and ReaxFF potentials, J. Chem. Phys. 160 (2024) 082501, https://doi.org/10.1063/5.0182460.
[81] C. Adamo, V. Barone, Exchange functionals with improved long-range behavior and adiabatic connection methods without adjustable parameters: the mPW and mPW1PW models, J. Chem. Phys. 108 (1998) 664–675, https://doi.org/10.1063/1.475428.
[82] C. Adamo, V. Barone, Toward reliable density functional methods without adjustable parameters: the PBE0 model, J. Chem. Phys. 110 (1999) 6158–6170, https://doi.org/10.1063/1.478522.
[83] M. Ernzerhof, G.E. Scuseria, Assessment of the Perdew–Burke–Ernzerhof exchange-correlation functional, J. Chem. Phys. 110 (1999) 5029–5036, https://doi.org/10.1063/1.478401.
[84] A.D. Becke, Density-functional thermochemistry. III. The role of exact exchange, J. Chem. Phys. 98 (1993) 5648–5652, https://doi.org/10.1063/1.464913.
[85] T.M. Henderson, A.F. Izmaylov, G.E. Scuseria, A. Savin, Assessment of a middle-range hybrid functional, J. Chem. Theory Comput. 4 (2008) 1254–1262, https://doi.org/10.1021/ct800149y.
[86] J.P. Perdew, A. Ruzsinszky, G.I. Csonka, L.A. Constantin, J. Sun, Workhorse Semilocal density functional for condensed matter physics and quantum chemistry, Phys. Rev. Lett. 103 (2009) 026403, https://doi.org/10.1103/PhysRevLett.103.026403.
[87] J.P. Perdew, Density-functional approximation for the correlation energy of the inhomogeneous electron gas, Phys. Rev. B 33 (1986) 8822–8824, https://doi.org/10.1103/PhysRevB.33.8822.
[88] J.-D. Chai, M. Head-Gordon, Long-range corrected hybrid density functionals with damped atom–atom dispersion corrections, Phys. Chem. Chem. Phys. 10 (2008) 6615, https://doi.org/10.1039/b810189b.
[89] V.F.D. Peters, J.A. Koskamp, D. Di Tommaso, M. Wolthers, Influence of solution stoichiometry on the thermodynamic stability of prenucleation FeS clusters, Phys. Chem. Chem. Phys. 27 (2025) 3115–3123, https://doi.org/10.1039/D4CP03758H.
[90] D. Rickard, A.P. Roberts, A. Navrotsky, Sedimentary Greigite formation, Am. J. Sci. 324 (2024) 13, https://doi.org/10.2475/001c.121855.
[91] D. Rickard, Aqueous metal–sulfide chemistry: complexes, clusters and nanoparticles, in: Dev. Sedimentol., Elsevier, 2012, pp. 121–194, https://doi.org/10.1016/B978-0-444-52989-3.00004-0.
[92] M. Wolthers, L. Charlet, P.R. van Der Linde, D. Rickard, C.H. van Der Weijden, Surface chemistry of disordered mackinawite (FeS), Geochim. Cosmochim. Acta 69 (2005) 3469–3481, https://doi.org/10.1016/j.gca.2005.01.027.
[93] W. Davison, N. Phillips, B.J. Tabner, Soluble iron sulfide species in natural waters: reappraisal of their stoichiometry and stability constants, Aquat. Sci. 61 (1999) 23–43, https://doi.org/10.1007/s000270050050.
[94] D. Rickard, Kinetics of FeS precipitation: part 1. Competing reaction mechanisms, Geochim. Cosmochim. Acta 59 (1995) 4367–4379, https://doi.org/10.1016/0016-7037(95)00251-T.
[95] M. Wolthers, S.J. Van der Gaast, D. Rickard, The structure of disordered mackinawite, Am. Mineral. 88 (2003) 2007–2015, https://doi.org/10.2138/am-2003-11-1245.
[96] S.A. Sanden, R. Yi, M. Hara, S.E. McGlynn, Simultaneous synthesis of thioesters and iron–sulfur clusters in water: two universal components of energy metabolism, Chem. Commun. 56 (2020) 11989–11992, https://doi.org/10.1039/D0CC04078A.
[97] S. Scintilla, D. Rossetto, M. Clémancey, J. Rendon, A. Ranieri, G. Guella, M. Assfalg, M. Borsari, S. Gambarelli, G. Blondin, S.S. Mansy, Prebiotic synthesis of the major classes of iron–sulfur clusters, Chem. Sci. (2025), https://doi.org/10.1039/D5SC00524H.
[98] D. Rossetto, L. Valer, N. Yeh Martín, G. Guella, Y. Hongo, S.S. Mansy, Prebiotic environments with Mg2+ and Thiophilic metal ions increase the thermal stability of cysteine and non-cysteine peptides, ACS Earth Space Chem. 6 (2022) 1221–1226, https://doi.org/10.1021/acsearthspacechem.2c00042.
[99] J.D. Toner, D.C. Catling, Alkaline lake settings for concentrated prebiotic cyanide and the origin of life, Geochim. Cosmochim. Acta 260 (2019) 124–132, https://doi.org/10.1016/j.gca.2019.06.031.

[100] J.D. Toner, D.C. Catling, A carbonate-rich lake solution to the phosphate problem of the origin of life, Proc. Natl. Acad. Sci. 117 (2020) 883–888, https://doi.org/10.1073/pnas.1916109117.
[101] L. Valer, D. Rossetto, S. Scintilla, Y.J. Hu, A. Tomar, S. Nader, I.O. Betinol, S. S. Mansy, Methods to identify and characterize iron–sulfur oligopeptides in water, Can. J. Chem. 100 (2022) 475–483, https://doi.org/10.1139/cjc-2021-0237.
[102] G.R. Helz, I. Ciglenečki, D. Krznarić, E. Bura-Nakić, Voltammetry of sulfide nanoparticles and the FeS(aq) Problem, in: Aquat. Redox Chem., American Chemical Society, 2011, pp. 265–282, https://doi.org/10.1021/bk-2011-1071.ch013.
[103] W. Davison, Comment on "Determination of metal (Bi)sulfide stability constants of Mn2+, Fe2+, Co2+, Ni2+, Cu2+, and Zn2+ by Voltammetric Methods,", Environ. Sci. Technol. 30 (1996) 3638–3639, https://doi.org/10.1021/es960420h.
[104] R. Hanscam, E.M. Shepard, J.B. Broderick, V. Copié, R.K. Szilagyi, Secondary structure analysis of peptides with relevance to iron–sulfur cluster nesting, J. Comput. Chem. 40 (2019) 515–526, https://doi.org/10.1002/jcc.25741.
[105] S. Scintilla, C. Bonfio, L. Belmonte, M. Forlin, D. Rossetto, J. Li, J.A. Cowan, A. Galliani, F. Arnesano, M. Assfalg, S.S. Mansy, Duplications of an iron–Sulphur tripeptide leads to the formation of a protoferredoxin, Chem. Commun. 52 (2016) 13456–13459, https://doi.org/10.1039/C6CC07912A.
[106] R.K. Szilagyi, R. Hanscam, E.M. Shepard, S.E. McGlynn, Natural selection based on coordination chemistry: computational assessment of [4Fe–4S]-maquettes with non-coded amino acids, Interface Focus 9 (2019) 20190071, https://doi.org/10.1098/rsfs.2019.0071.
[107] S. Fawcett, Reactions of iron-sulfur clusters in proteins. http://purl.org/dc/dcmitype/Text, University of Oxford, . https://ora.ox.ac.uk/objects/uuid:87b10a8e-67a8-476b-ae20-49e6892051f5 (accessed September 15, 2025).
[108] P. D'Angelo, M. Benfatto, Effect of multielectronic configurations on the XAFS analysis at the Fe K edge, J. Phys. Chem. A 108 (2004) 4505–4514, https://doi.org/10.1021/jp0499732.
[109] D. Coucouvanis, D. Swenson, P. Stremple, N.C. Baenziger, Reaction of [Fe(SC6H5)4]2- with organic trisulfides and implications concerning the biosynthesis of ferredoxins. Synthesis and structure of the [(C6H5)4P]2Fe2S12 complex, J. Am. Chem. Soc. 101 (1979) 3392–3394, https://doi.org/10.1021/ja00506a050.